

# Experimental Analysis and Modeling for Reciprocating Wear Behavior of Nanocomposite Coatings

Mian Hammad Nazir<sup>1</sup>, Zulfiqar Ahmad Khan<sup>1\*</sup>, Adil Saeed<sup>1</sup>, Vasilios Bakolas<sup>2</sup>, Wolfgang Braun<sup>2</sup>, Rizwan Bajwa<sup>1</sup>

<sup>1</sup>NanoCorr Energy and Modelling Research Group (NCEM), Bournemouth University Talbot Campus, Poole, Dorset, BH12 5BB, UK

\*Email: [zkhan@bournemouth.ac.uk](mailto:zkhan@bournemouth.ac.uk)

<sup>2</sup>Advanced Bearing Analysis Schaeffler Technologies AG & Co. KG, 91074 Herzogenaurach, Germany

## Abstract

This paper presents the study of wear responses of nanocomposite coatings with a steel ball under oscillating-reciprocating state. Nanocomposite coatings for this study include: Nickel-Alumina (Ni/Al<sub>2</sub>O<sub>3</sub>), Nickel-Silicon Carbide (Ni/SiC), Nickel-Zirconia (Ni/ZrO<sub>2</sub>) and Ni/Graphene. Ni/ZrO<sub>2</sub> exhibited maximum wear rate followed by Ni/SiC, Ni/Al<sub>2</sub>O<sub>3</sub> and Ni/Graphene respectively which was also assured by Scanning Electron Microscopy (SEM) micrographs, grain sizes, hardness, porosity, surface stresses, frictional coefficients behaviours and “U-shaped” wear depth profiles. The “U-shaped” profiles were utilised to calculate the energy distribution (Archard factor density) along the interface. A novel mechano-wear model incorporating the energy distribution equations with the mechanics equations was developed for analysing the effects of intrinsic mechanical properties (such as grain sizes, hardness, porosity, surface stresses of the nanocomposite coatings) on the wear response. The predictions showed close agreement with the experimental results. In conclusion Ni/Graphene exhibited better anti-wear properties compared to other nanocomposite coatings. The high anti-wear behaviour of Ni/Graphene composite is due to enhanced strengthening effects in the presence of graphene. The importance of this work is evident from various industrial applications which require reliable modelling techniques to predict coatings failures due to wear. This work will bring significant impact to precision manufacturing, wind turbine industries, automotive, locomotive and aerospace in overcoming critical wear failures.

**Keywords:** Reciprocating wear; Nanocomposite coatings; Modelling; Simulation

## 1. Introduction

Research interests in preparation and nanoscale properties of nanocomposite materials with grain size of both matrix and dispersed nano particles less than 100 nm have increased to address specific demands of high wear resistance and low friction coefficient for current advanced technological applications, for example automotive, defence and aerospace [1, 2]. Nowadays, the nanostructured design by dispersion of nano particles into the matrix has proved to be ground-breaking tool for attaining the enhanced thermal, electrical, optical and mechanical properties compared to conventional metallic materials [3-5]. Normally, electrodeposition involves only one-step deposition process under normal room conditions [6]. The well-established technique offers significant low-cost, reliability and environmental advantages over the previously used evaporation technology [8]. Electrodeposition of various nickel based nanocomposite coatings have been performed by using various types of nano particles including Al<sub>2</sub>O<sub>3</sub>, SiC, ZrO<sub>2</sub>, Graphene and TiO<sub>2</sub> [7-11]. In-depth experimental analyses on fretting wear of electrodeposited nickel-Al<sub>2</sub>O<sub>3</sub>, nickel-SiC, nickel-ZrO<sub>2</sub> and nickel-Graphene (GPL) nanocomposite coatings were performed [12, 13] and it was found that nickel-graphene coating showed better fretting wear resistance. However, little work has been concerned with the development of predictive models for analysing the fretting wear of nanocomposite coatings.

Fretting wear has been broadly studied in the past few years because of its extreme impact on structural reliability [14-18]. Fretting wear in various metallic materials and alloys can now be predicted, however predicting the fretting wear behaviour of nanocomposite coatings needs further research. The prediction of various intrinsic mechanical parameters for example surface stress, porosity and grain size on the fretting wear behaviour of nanocomposite coatings has always been a challenge. This is revealed by large number of wear models and the problems in predicting the fretting wear of nanocomposite coatings with loading parameters like

pressure and friction coefficient. Latest research shows a growing interest in improved wear formulation [19-23].

In the present work, novel mechano-wear equations have been developed which integrate the concepts of Archard theory and mechanics for quantifying eigenstress-dependent fretting wear processes for nanocomposite coatings. The study utilises gross slip fretting conditions, concentrating on metal interfaces. Such condition involves damage which is primarily regulated by abrasion. Our group is conducting similar research on nanocomposite coatings [24-32].

This study is conducted to provide answers to the following key questions within the context of industrial applications underpinned by multidisciplinary understanding and approach: (i) How the generic wear behaviour of nanocomposite/steel tribo-couples can be formalised by using a well-known Archard equation integrated with mechanics equations?, (ii) How can the influences of intrinsic mechanical parameters of the nanocomposite coatings on the wear response be analysed?, (iii) What measures can be taken to predict the wear depth kinetics, similarly which intrinsic mechanical properties influence wear depth kinetics the most? and (iv) How can the reliability of wear predictions be validated by detailed comparison with the experimental findings?

## 2. Experimental study

### 2.1. Sample Preparation

Nanocomposite coatings; Ni/Al<sub>2</sub>O<sub>3</sub>, Ni/SiC, Ni/ZrO<sub>2</sub> and Ni/Graphene (GPL) were deposited on steel substrate. Electrodeposition technique was adopted to deposit coatings on substrate. The thickness of all the coatings was kept constant as  $h_c = 10 \mu\text{m}$ . All the samples had dimensions as 30mm×10mm×3mm and the substrate roughness was kept as 0.05  $\mu\text{m}$ . Ultrasonic treatment was used for substrate conditioning before coating deposition.

Nanocomposite coatings were electrodeposited by using the solutions which were composed of Nickel(II) Sulfate Hexahydrate (265 g/L), Nickel(II) chloride (48 g/L) and Boric acid (31 g/L). These solutions were ultrasonically dispersed with four various types of nanoparticles. The amount of nanoparticles was set as 20 g/L with sizes as: Nano ZrO<sub>2</sub> (100 nm), Nano SiC (40-50 nm), Nano Al<sub>2</sub>O<sub>3</sub> (30-40 nm), and Graphene platelets (5-7 nm). For better particle suspension before the coating deposition, the solution was magnetically stirred overnight and the solutions' pH value was maintained between 4.0 to 4.5 by NaOH or diluted H<sub>2</sub>SO<sub>4</sub>. The electrodeposition current density and pulse on-off time was set as 5 A/dm<sup>2</sup> and 30-90 ms respectively. Anode was made of nickel metal 8.20 mm thick while 80 mm in diameter steel disc acted a cathode.

### 2.2. Tribo-Testing

Tribological properties of electrodeposited nanocomposite coatings were studied using a modified linearly reciprocating sliding contact tribometer (Plint TE57/77) as shown in Fig. 1. The tribometer consisted of lower fixed electrodeposited specimen plate and upper 100Cr6 steel ball (H: 740HV, E: 210GPa and  $\nu$ : 0.3) with R = 4.8 mm radius. All tribo-tests were performed with immersed deionised water lubrication. The normal force P was set as 15 N. The sliding velocity and frequency were set as 0.05 m/sec and 10 Hz respectively. Constant sliding amplitudes  $\delta_g$  was used. The wear depth profile along x-axis relative to  $x = 0$  was represented as  $h(x)$ . The left side displacement relative to  $x = 0$  was  $-\delta$  whereas the right-side displacement was  $+\delta$  (see Fig. 1). The selected tribo-conditions guaranteed boundary lubrication regime and complete data retrieval prior to coating failure. Tribological tests for each type of coatings were repeated at least three times. Note that all the coatings were polished prior to tribological testing in order to minimise the influence of any bulging particles.

Friction coefficient data was retrieved through COMPEND software with Plint-TE 57/77 tribometer. The failure mechanism of coatings and elements content in wear tests were studied by using SEM (Scanning Electron Microscope) and EDS (Energy-dispersive X-ray Spectroscopy) analyses, respectively. The average grain size of nanocomposite coatings was measured by using an optical microscopy (OM) with application software. The surface roughness and loss of coating material in wear testing was examined by using a three-dimensional white-light interferometer and measured wear volume was used to calculate specific wear rate [12].

The internal stresses of coatings pre and post wear tests were measured by using a conventional beam-bending method [33]. The internal stress in coating was evaluated by using the following equilibrium equation [34]:

$$\sigma_c = 4E_3 s^2 D / [3L^2 (1 - \nu_s) h_c]$$

1

where  $E_3$  (200 GPa) is the steel substrate Young's modulus;  $s$  is the steel substrate thickness;  $\nu_s$  (0.29) is the steel substrate Poisson's ratio;  $L$  is the substrate segment length;  $h_c$  is the coating thickness; and  $D$  is the central deflection. The measured internal stresses of Ni/Al<sub>2</sub>O<sub>3</sub>, Ni/SiC, Ni/ZrO<sub>2</sub> and Ni/GPL are 0.9 GPa, 2.0 GPa, 3.0 GPa and 0.4 GPa respectively. The measured results for all the coatings are shown in Table 1.

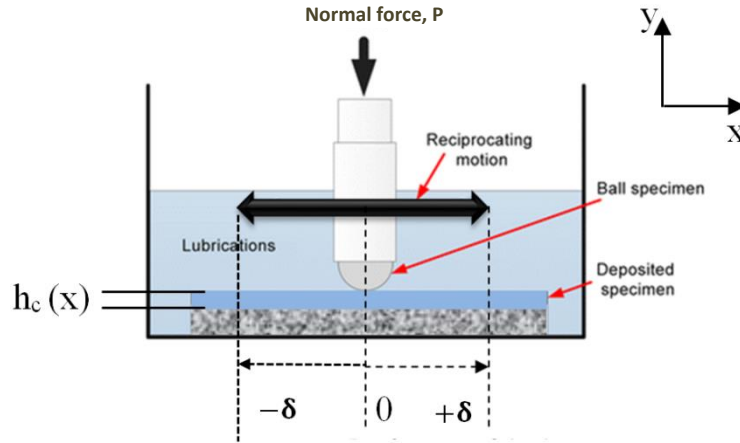


Figure 1. Schematic diagram of reciprocating sliding contact testing [31]. The ball in contact with the degraded coating having a wear depth of  $h(x)$  along  $x$ -axis while displacement is shown as  $-\delta$  (left of centre) and  $+\delta$  (right of centre).

Table 1. Measured properties of all the nanocomposite coatings

No.	Ni/Al <sub>2</sub> O <sub>3</sub>	Ni/SiC	Ni/ZrO <sub>2</sub>	Ni/GPL
$R_a$ (nm)	$0.15 \pm 0.12$	$0.19 \pm 0.08$	$0.30 \pm 0.2$	$0.07 \pm 0.04$
Hardness (GPa)	$452 \pm 25$	$410 \pm 21$	$390 \pm 18$	$480 \pm 24$
Internal stress (GPa), $\sigma_c$	+ 0.9	+ 2.0	+ 3.0	+ 0.4
<b>Tribo-test conditions</b>				
Normal force	15 N			
Sliding speed	0.05 m/sec			
Frequency	10 Hz			
Stroke length	5 mm			
Lubrication	Deionised water			

## 2.3. Experimental Observations

### 2.3.1. Surface Morphology of Nanocomposite Coatings

In Table 2, the pre-test SEM micrographs demonstrate the microstructure morphology of electrodeposited nanocomposite coatings while pre-test EDS results identify the elements and their concentration in all the coatings. As shown in the top image of pre-test SEM cell of Table 2, all coatings exhibits the typical hexagonal pyramid grain structure which is consistent with previous investigations by other researchers [35-38].

The pre-test particle size and their distribution was analysed by cross sectional SEM images in Fig. 2 showing the largest sized particles in Ni/ZrO<sub>2</sub> and the smallest sized particles, uniformly distributed in huge amount in

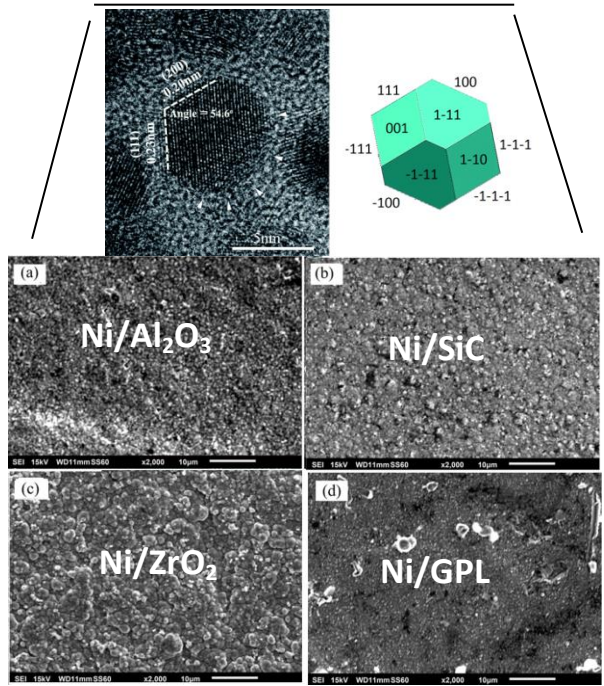
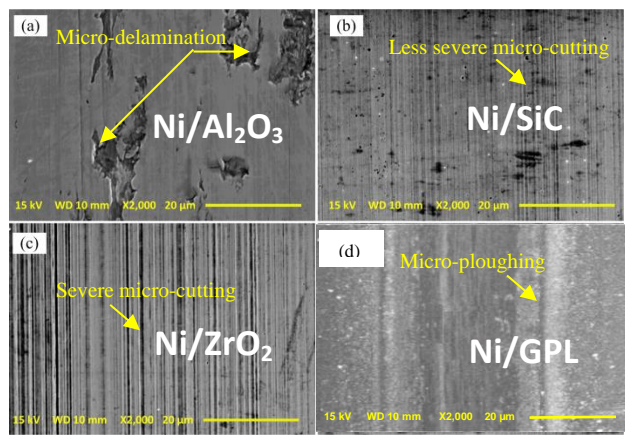
Ni/GPL. The more magnified SEM images of coatings surface in Fig. 3 revealed that Ni/ZrO<sub>2</sub> exhibited largest pore sizes followed by Ni/SiC and Ni/Al<sub>2</sub>O<sub>3</sub>. Ni/GPL however showed pore free surface.

Next the pre-test grain size measurement was performed as shown in Fig. 4. The figure shows that the largest average grain size was observed in Ni/ZrO<sub>2</sub> ( $19.68 \pm 2$  nm) while the smallest average grain size was found in Ni/GPL ( $11.21 \pm 9$  nm). Wear properties are significantly influenced by grain structure [39]. The grain size of Ni/GPL was also observed to be extremely fine which resulted in better wear properties of Ni/GPL compared to the rest of the coatings.

Post-test SEM micrographs of the worn surface morphologies of nanocomposite coatings after tribo-testing are shown in Table 2. It can be seen that mainly micro-cutting, micro-delamination and micro-ploughing wear mechanisms are observed on the worn wear tracks. Micro-cutting is characteristics of plastic deformation [40]. The largest parallel micro-grooves can be seen on the worn surfaces of Ni/ZrO<sub>2</sub> followed by Ni/SiC indicating plastic deformation in both as shown in Table 2 (post-test, SEM (b and c)). For the case of Ni/Al<sub>2</sub>O<sub>3</sub> the wear mechanism is micro-delamination and for Ni/GPL, the wear mechanism is micro-ploughing as shown in Table 2 (post-test, SEM (a and d)). The removal of Ni/Al<sub>2</sub>O<sub>3</sub> material due to micro-delamination wear mechanism caused high friction coefficient value which will be discussed in the coming section (Fig. 11).

Post-Test EDS elemental analyses of worn surfaces are shown in Table 2. The presence of nanoparticles (Al, Si, Zn and GPL) spectrum peaks confirmed their influence on the tribological properties. The relative stronger peak of Fe element in Ni/GPL composite indicated that many wear debris from counter steel ball transferred on wear track due to higher micro hardness of Ni/GPL compared to the rest of the coatings (i.e. Ni/GPL = 480 HV, Ni/Al<sub>2</sub>O<sub>3</sub> = 452 HV, Ni/SiC = 410 HV and Ni/ZrO<sub>2</sub> = 390 HV). During fretting wear, the counter steel ball surface showed the highest wear weight loss against Ni/GPL as shown in Fig. 5 (d) compared to the rest (Fig. 5 (a-c)). This clearly indicates the well-matched hardness of Ni/GPL as with the counter steel ball (740 HV) compared the rest of coatings.

Table 2. Pre and Post exposure SEM and EDS results of nanocomposite coatings

	Pre - Test	Post – Test
SEM		

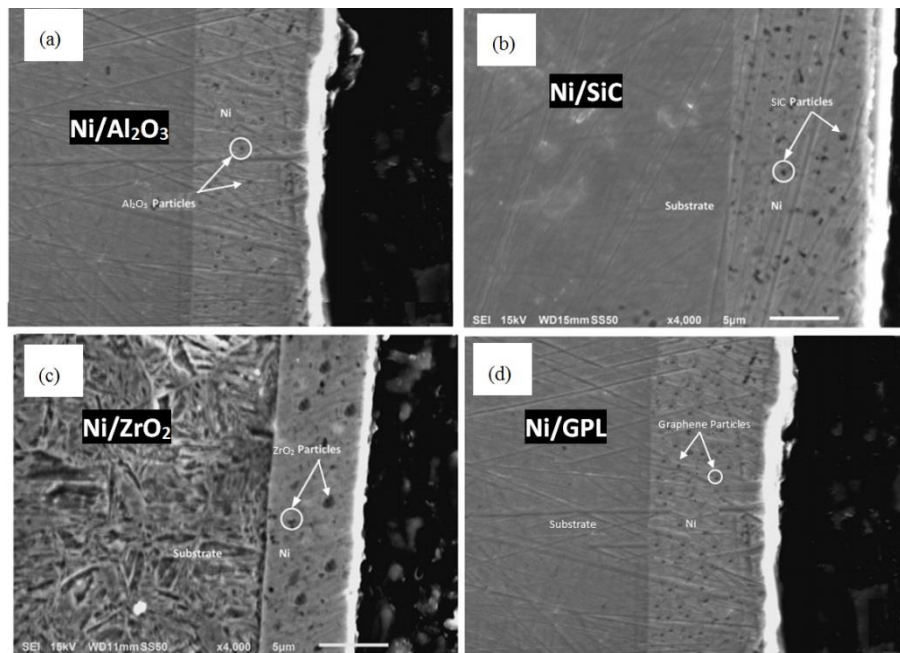
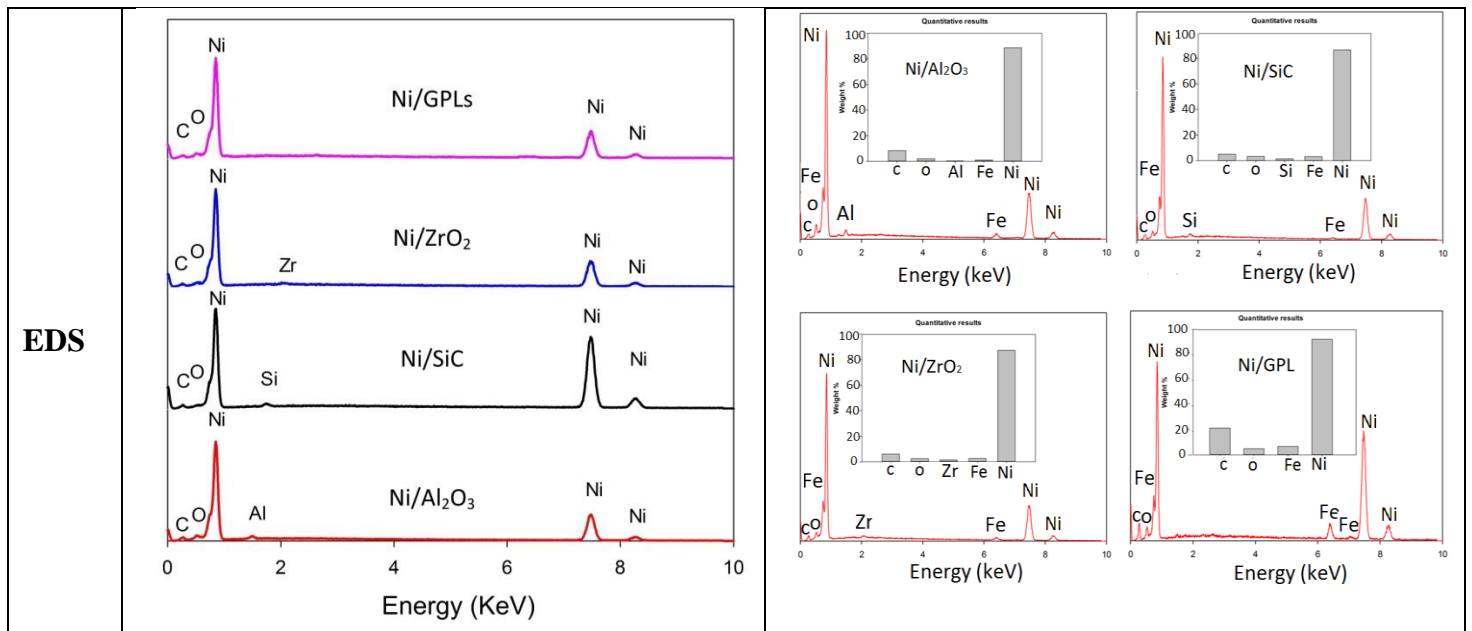


Figure 2. Pre-test cross-sectional SEM micrographs of incorporated nanoparticle distributions in the nickel-based composite coatings: (a) Ni/Al<sub>2</sub>O<sub>3</sub> (b) Ni/SiC (c) Ni/ZrO<sub>2</sub> and (d) Ni/GPL.



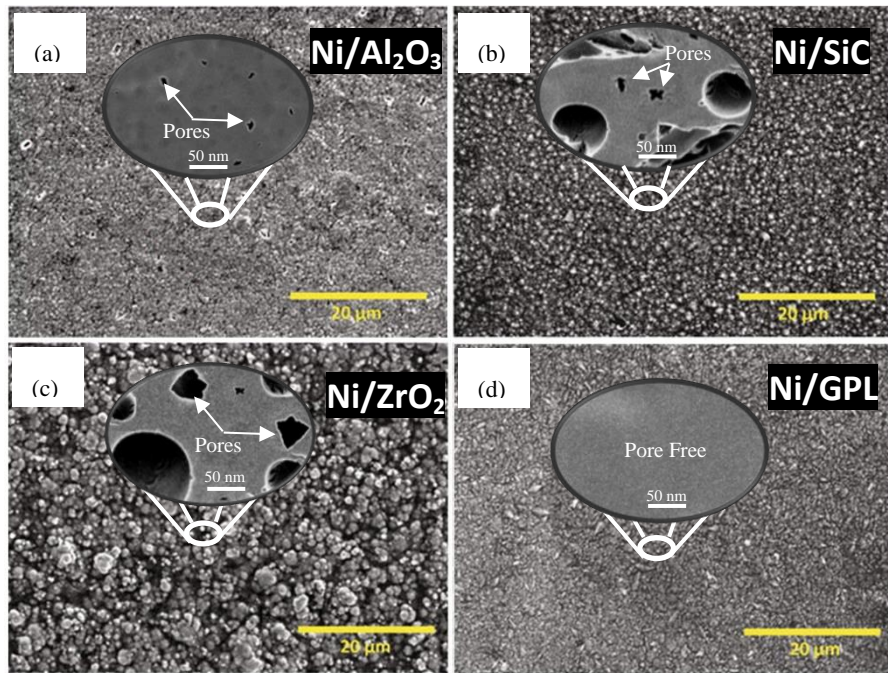
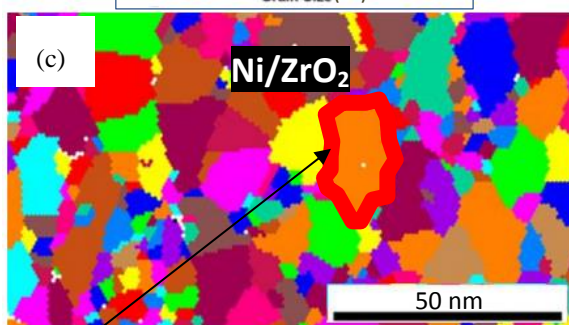
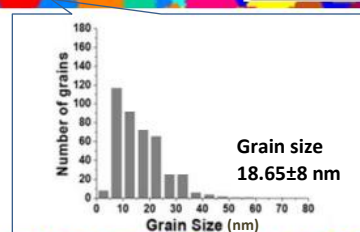
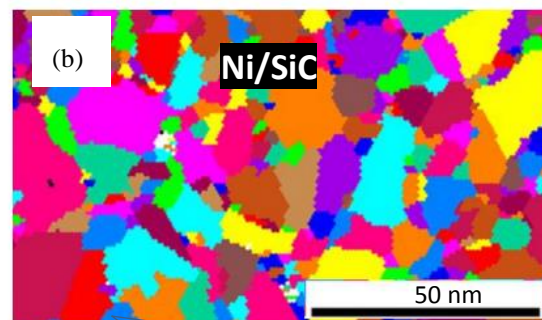
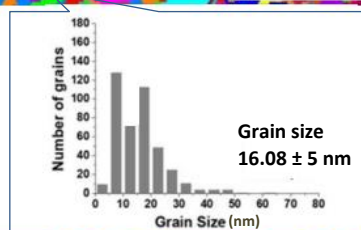
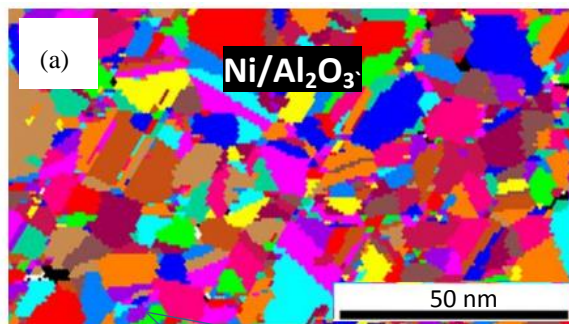
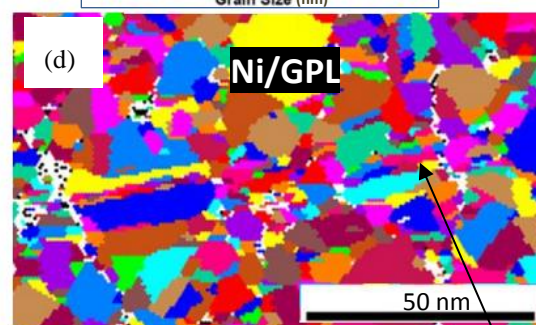
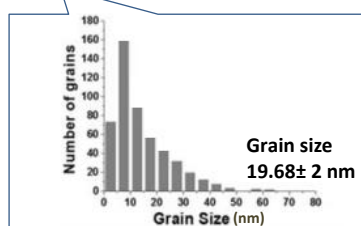


Figure 3. SEM images showing porosity in the nickel-based composite coatings: (a) Ni/Al<sub>2</sub>O<sub>3</sub> (b) Ni/SiC (c) Ni/ZrO<sub>2</sub> and (d) Ni/GPL.



Large Grain



Refined grains

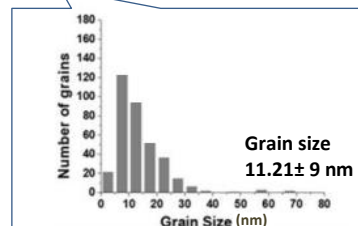


Figure 4. Pre-test grain size maps of the (a) Ni/Al<sub>2</sub>O<sub>3</sub> (b) Ni/SiC (c) Ni/ZrO<sub>2</sub> and (d) Ni/GPL

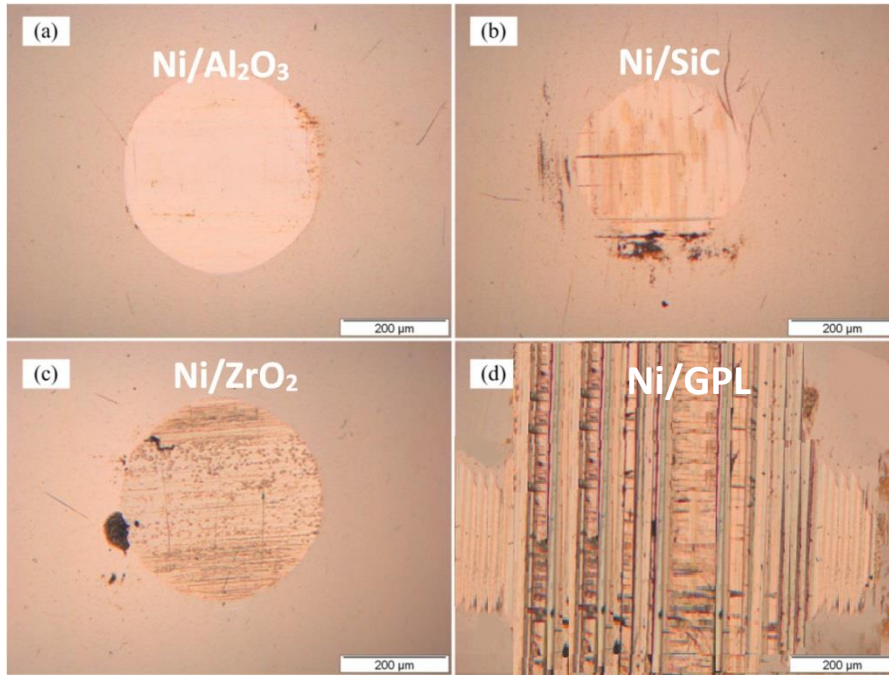


Figure 5. Optical photographs of worn tracks of 100Cr6 steel ball sliding against: (a) Ni/Al<sub>2</sub>O<sub>3</sub> (b) Ni/SiC (c) Ni/ZrO<sub>2</sub> and (d) Ni/GPL.

### 2.3.2. Wear Rates, Surface Stress and Frictional Coefficients Behaviours

Fig. 6 presents the wear rate outcomes of all the electrodeposited nanocomposite coatings. A well-known Archard equation is used to compute the wear rate. For this, wear volume ( $V$ ) is taken as a function of Archard factor ( $\sum W$ ). The Archard factor is the product of normal force  $P_L$  (N) and the total sliding displacement  $\delta$  (m). In other words Archard factor is also defined as energy dissipated during fretting cycle.

Fig. 6 shows a rising trend of nanocomposite coatings wear volume ( $V$ ) with increasing Archard factor  $\sum W$  for sliding condition [20, 41]. For these rising trends, the corresponding wear rate coefficients  $K_v$  are deduced by using regression [41]:

$$K_v = \frac{\Delta V}{\Delta (\sum W)} = \frac{\Delta V}{\Delta (\sum_{i=1}^Z P_{(i)} \delta g_{(i)})} \quad 2$$

Where  $i$  is the corresponding fretting cycle.

Table 3 presents the  $K_v$  values and the corresponding averaged friction coefficients.

As can be seen from Table 3 that Ni/ZrO<sub>2</sub> composite exhibits the maximum wear rate coefficient. In comparison to Ni/ZrO<sub>2</sub> a reduction of 14 % and 43 % was observed in Ni/SiC and Ni/Al<sub>2</sub>O<sub>3</sub> composites respectively. When compared with Ni/GPL a maximum reduction of 48 % was achieved in the wear rate coefficient.

It is interesting to note that Ni/GPL composite showed the best wear resistant properties.



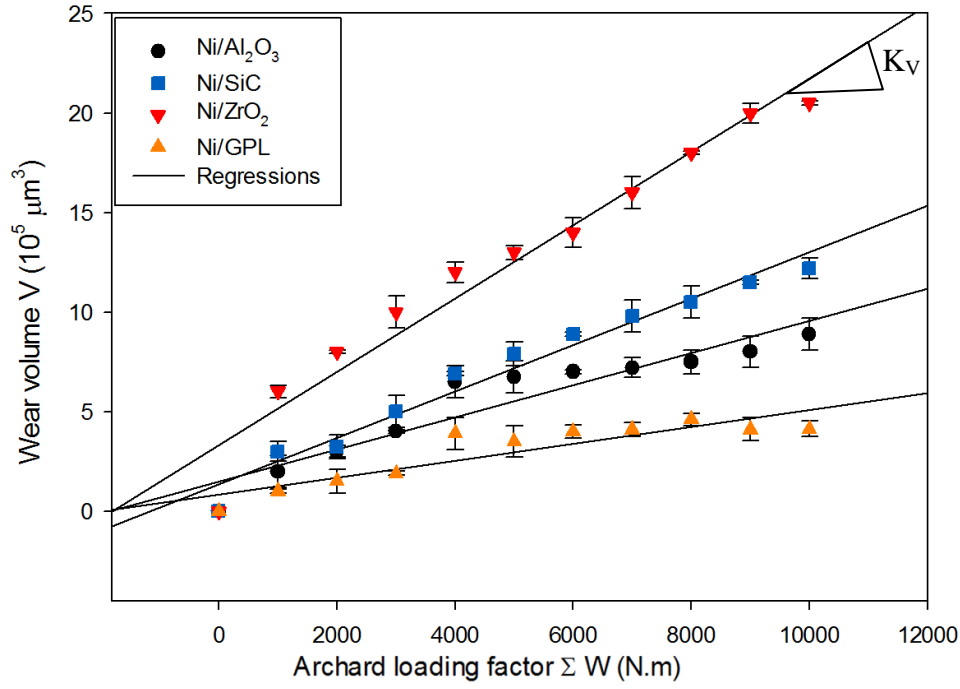


Figure 6. The wear volume as a function of  $\Sigma W$  ( $R = 4.8$  mm, deionised water lubricant,  $f = 10$  Hz,  $P = 15$  N,  $\delta = \pm 25$  to  $\pm 50 \mu\text{m}$ ,  $i: 1-10,000$ ).

Table 3. Wear rate coefficient  $K_v$  (regression lines) and friction coefficient of analysed nanocomposite coatings against steel ball (4.8 mm radius steel ball, deionised water lubricant,  $f = 10$  Hz,  $P = 15$  N,  $\delta = \pm 25$  to  $\pm 50 \mu\text{m}$ ,  $i: 1-10,000$ ).

Coating	Wear rate coefficients $K_v (\mu\text{m}^3 (\text{Nm})^{-1})$	Averaged friction coefficient $\bar{\mu}$
Ni/Al <sub>2</sub> O <sub>3</sub>	81	0.24
Ni/SiC	117	0.15
Ni/ZrO <sub>2</sub>	185	0.20
Ni/GPL	42	0.16

The wear rates coefficients  $K_v$  and averaged friction coefficient  $\bar{\mu}$  (in Table 3) for all nanocomposite coatings can be compared with the corresponding measured coating hardness (HV). The measured hardness values for all the coatings are shown in Fig. 7. The hardness measured by using nano-indentation showed highest hardness for Ni/GPL and lowest for Ni/ZrO<sub>2</sub> as shown in Fig. 7.

It is evident in Fig. 8 (and also from Archard Wear Law [42]) that the wear rate coefficients  $K_v$  of all coatings linearly decreased with increasing hardness i.e.  $K_v \propto \frac{1}{\text{HV}}$  while averaged friction coefficient  $\bar{\mu}$  also showed the decreasing behaviour except Ni/Al<sub>2</sub>O<sub>3</sub>. Ni/Al<sub>2</sub>O<sub>3</sub> showed higher averaged friction coefficient due to the production of wear-debris as a result of micro-delamination which can be clearly seen in AFM images in Fig. 9.

Fig. 9 illustrates that Ni/ZrO<sub>2</sub> showed severe micro-cutting deformation compared to Ni/SiC which showed less severe micro-cutting while Ni/Al<sub>2</sub>O<sub>3</sub> showed micro-delamination and Ni/GPL showed micro-ploughing deformation. Relating these deformations (Fig. 9) with their corresponding wear rate coefficients  $K_v$  (Fig. 8) establishes that for the case of Ni-based composite coatings, micro-cutting (in Ni/SiC and Ni/ZrO<sub>2</sub>) corresponds to the high wear rate coefficients ( $185$  and  $117 \mu\text{m}^3 (\text{Nm})^{-1}$ ) with low hardness ( $390 \pm 18$  and  $410 \pm 21$  GPa) while micro-ploughing in Ni/GPL corresponds to lowest wear rate coefficient ( $42 \mu\text{m}^3 (\text{Nm})^{-1}$ ) with highest hardness ( $480 \pm 24$  GPa) followed by micro-delamination in Ni/Al<sub>2</sub>O<sub>3</sub> with wear rate coefficient ( $81 \mu\text{m}^3 (\text{Nm})^{-1}$ ) and hardness ( $452 \pm 25$  GPa).

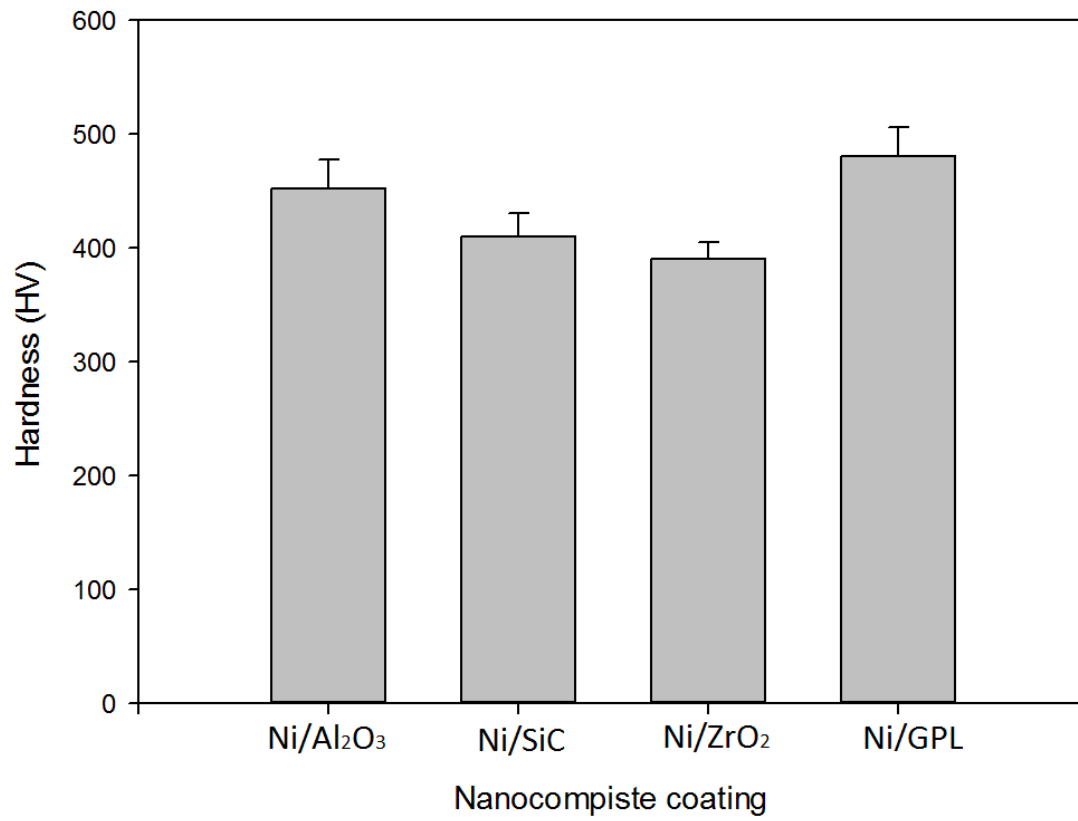


Figure 7. The hardness of nanocomposite coatings

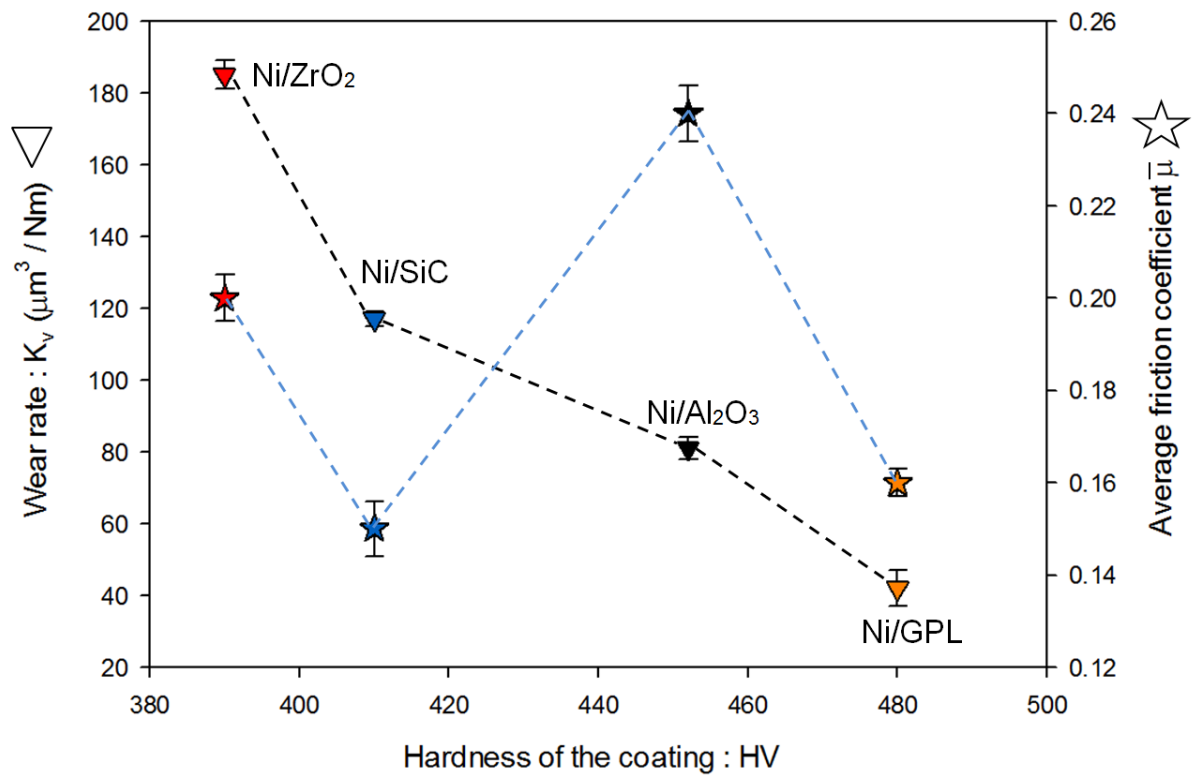


Figure 8. Wear rate coefficient and averaged friction coefficients (Table 3) with increasing hardness HV; ( $R = 4.8$  mm, deionised water lubricant,  $f = 10$  Hz,  $P = 15$  N,  $\delta^* = \pm 25$  to  $\pm 50 \mu\text{m}$ ,  $i: 1-10,000$ ).

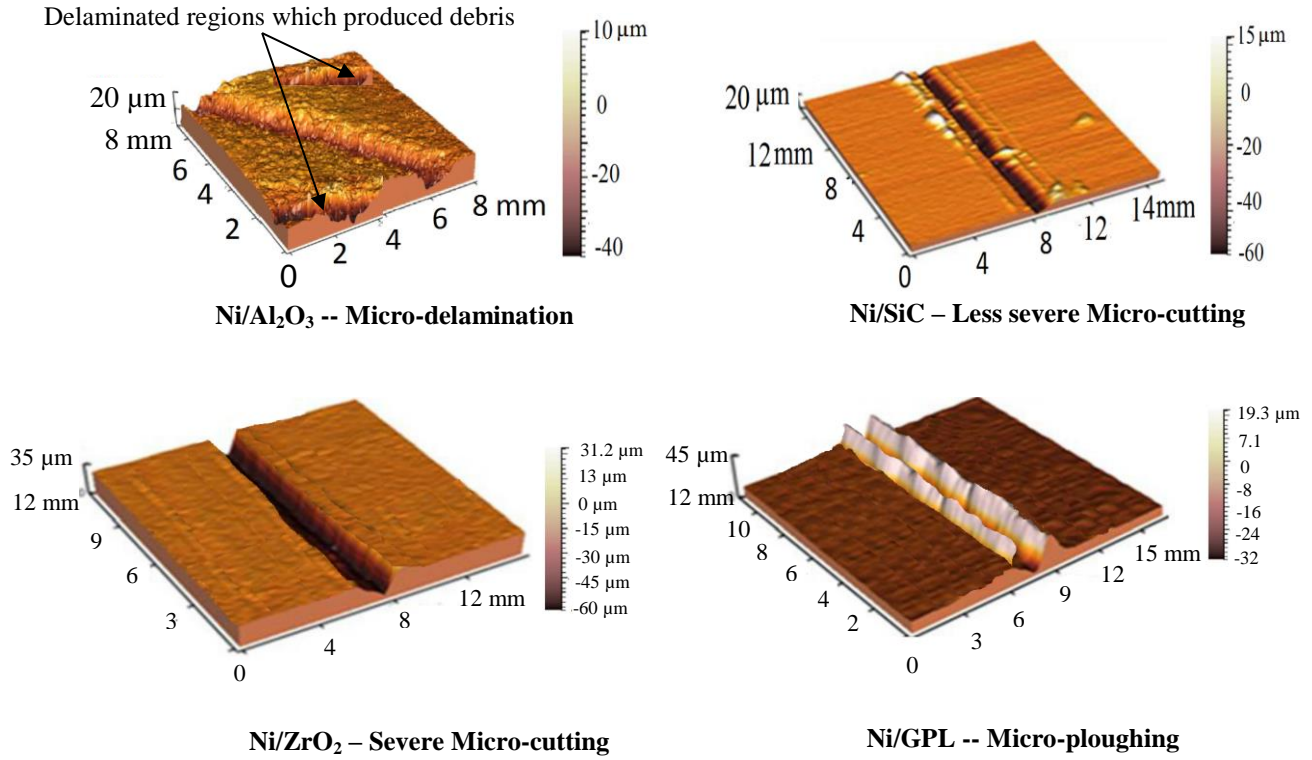


Figure 9. Types of deformations occurred during tribo-testing

The addition of both intrinsic stresses (due to grain boundary) and extrinsic stresses (due to thermal mismatch coefficient of coating and substrate) is responsible for total internal stress in nanocomposite coatings. As the deposition of coating system was performed under ambient conditions therefore it is likely that extrinsic stresses are negligible. The results reveal that the tensile stress increases the tendency of crack initiation and propagation [43]. The experimental conditions are summarised in Table 1 showing that all coatings exhibit tensile stress. The surface stress of all coatings together with normalised surface contact distance  $x/a_H$  is shown in Fig. 10. The dashed lines are the stress distribution without tribo-test.

It can be seen from Fig. 10 that in the Ni/ZrO<sub>2</sub> with an internal stress of +3.0 GPa, the maximum tensile stress at the rear contact point ( $x/a_H = -4$ ) increased from 0.6 to 3.8 GPa. This means that the internal tensile stress in Ni/ZrO<sub>2</sub> increased the surface tensile stress of Ni/ZrO<sub>2</sub>. Such behaviour resulted in cracking in the coating surface which can be seen in the form of severe micro-cutting in Fig. 9. Likewise Ni/SiC showed lower increase in rear contact stress (2.05 GPa) followed by Ni/Al<sub>2</sub>O<sub>3</sub> (1.5 GPa) and Ni/GPL (0.4 GPa). Relating stress behaviours of coatings with their grain sizes (in Fig. 4) clearly reflects the fact that the fracture failure (cracking) of coatings depends on their grain size and increases with increasing grain size. Refined grains account for higher hardness (e.g. Ni/GPL), better yield strength and ultimate tensile strength which limits fracture failure and in turn reduces wear deformation [44].

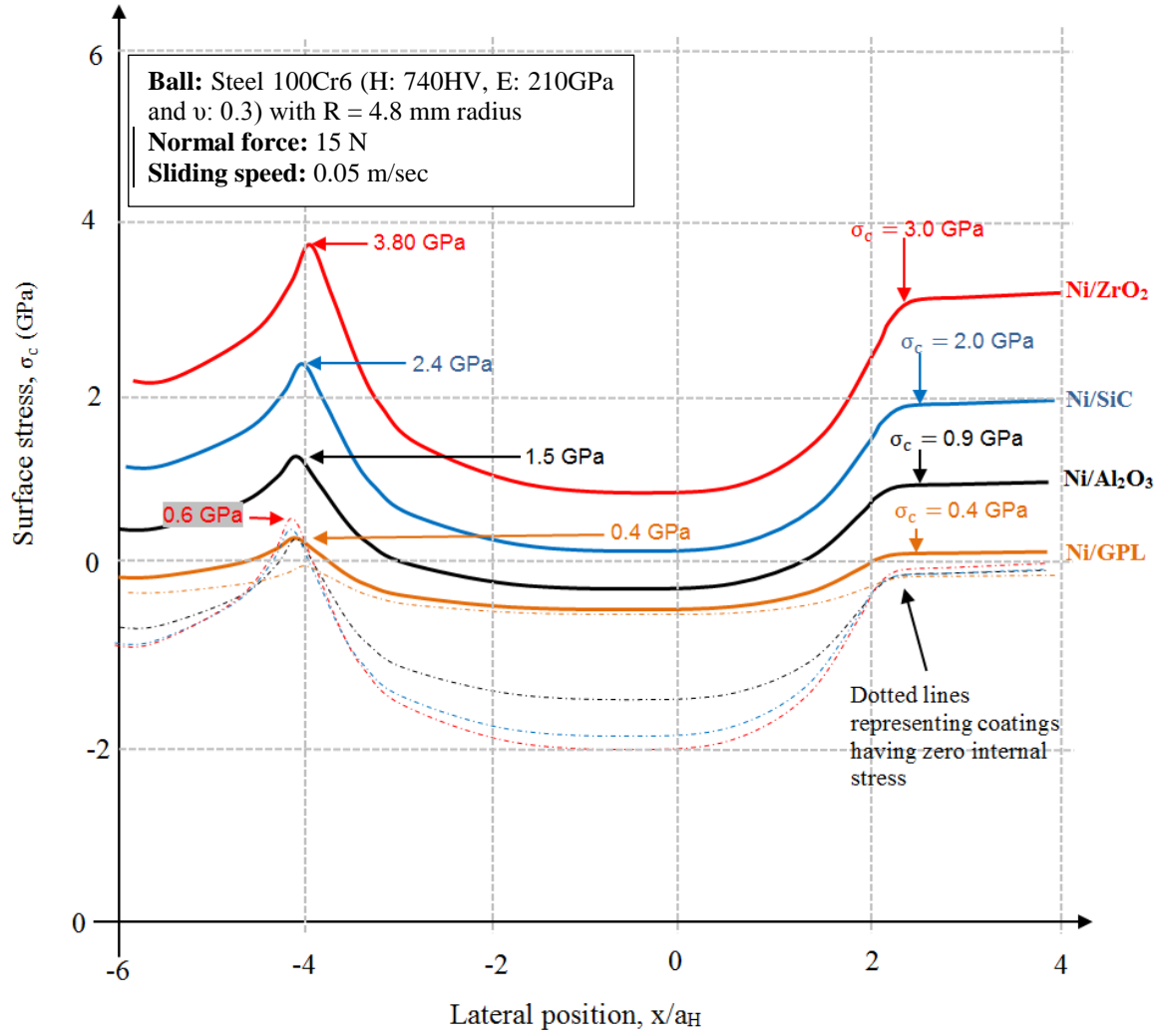


Figure 10. The surface stress of all coatings along the normalised surface contact distance  $x/a_H$

Likewise, the averaged friction coefficients corresponding to wear rates are also shown in Fig. 11. The highest averaged friction coefficient was observed for Ni/Al<sub>2</sub>O<sub>3</sub> which is related to the micro-delamination behaviour (Fig. 9) producing wear debris increasing the friction coefficient [45]. Ni/GPL showed the third lowest averaged friction coefficient  $\bar{\mu}$  after Ni/ZrO<sub>2</sub> because the huge amount of graphene in the Ni/GPL (Fig. 2) resulted in the formation of graphene tribo-film; consequently the averaged friction coefficient was reduced. Ni/SiC showed the lowest value as SiC reacted with water in sliding and formed soft surface layers of SiO<sub>2</sub> and its hydride which significantly reduced the wear rate of Ni/SiC [46]. Fig. 11 shows the friction coefficient  $\mu$  for all the coatings as a function of Archard factor ( $\Sigma W$ ) displaying a clear stabilisation in the friction coefficient after certain point except Ni/Al<sub>2</sub>O<sub>3</sub>, the reason for which is the production of wear debris, resisting stabilisation.



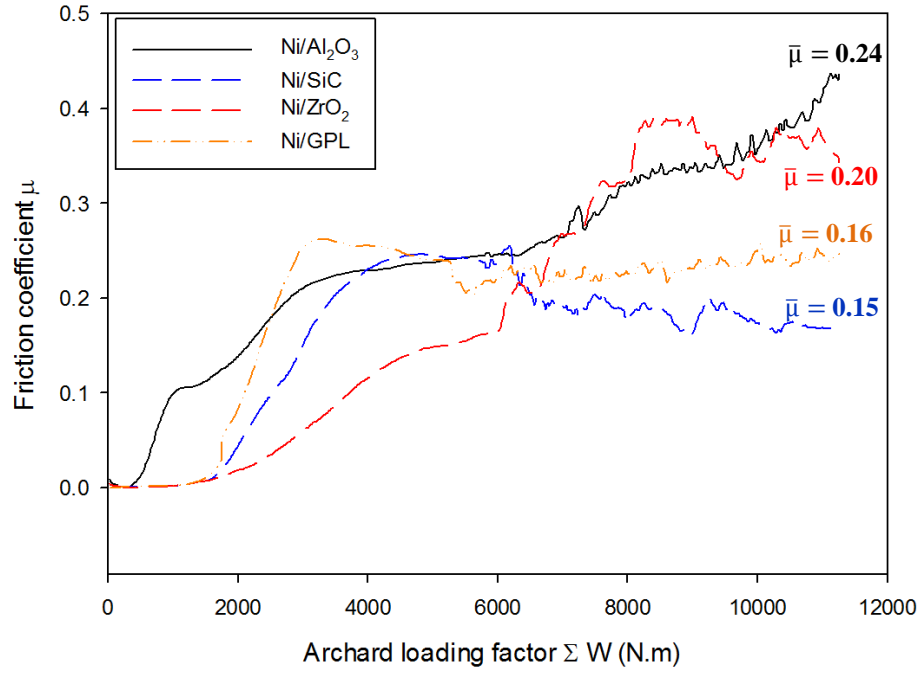


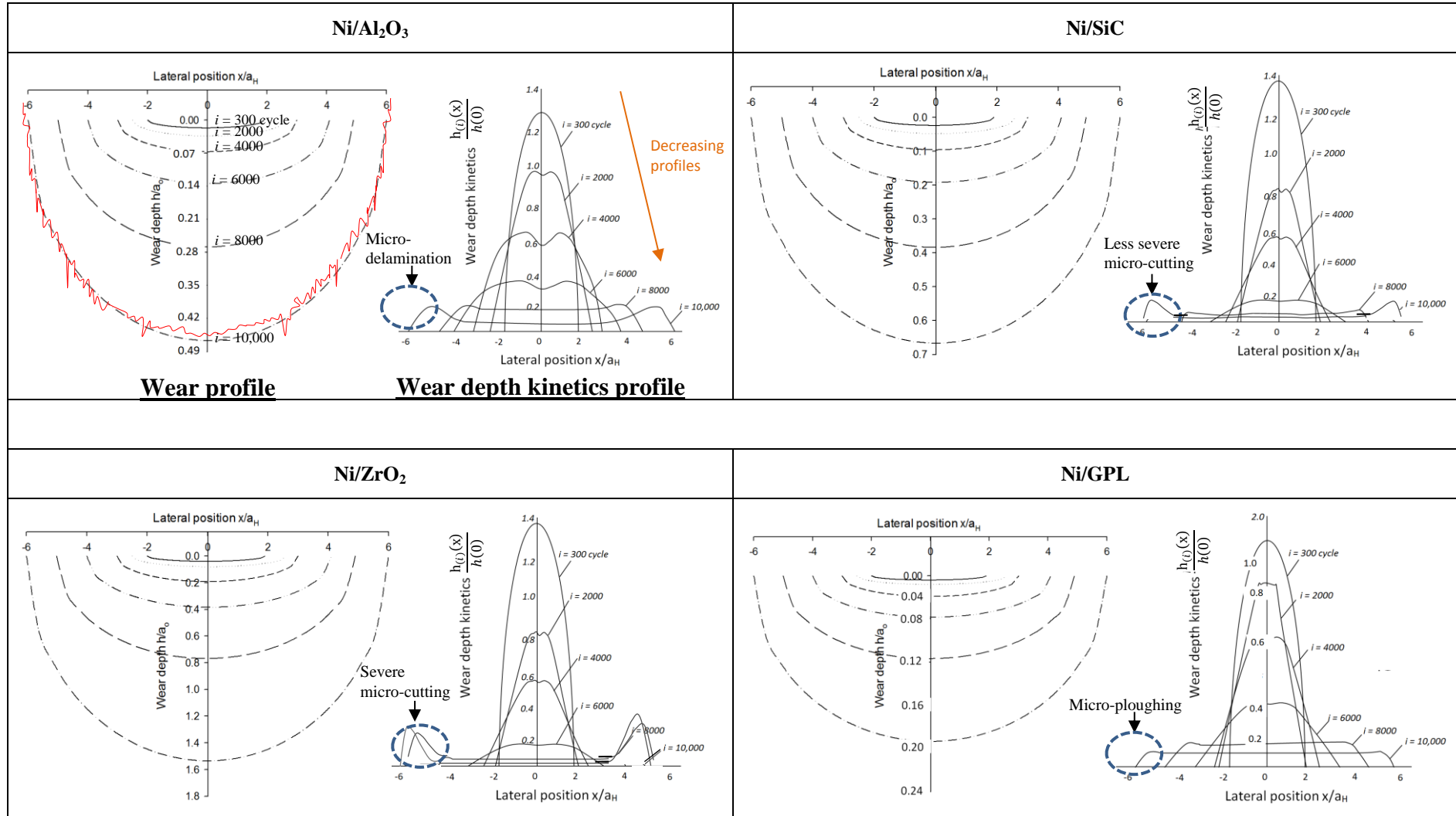
Figure 11. Variation in average friction coefficient of different types of electrodeposited composite coatings sliding against 100Cr6 steel ball

### 2.3.3. Wear Profiles and Wear Depth Kinetics Profiles

Figures in Table 4 plot the evolution of normalised ‘wear profiles’ (figures on left in each cell) and normalised ‘wear depth kinetics profiles’ (figures on right in each cell) at different stages of degradation for all the coatings. An even “U-shaped” wear profiles with the centre of the interface located at  $x = 0$  are observed. The highest depth of wear profile is always located at the centre. As evident from Table 4 that Ni/ZrO<sub>2</sub> exhibited largest normalised wear depth ( $= 1.5$ ) at  $i = 10,000^{\text{th}}$  cycle compared to Ni/SiC ( $= 0.68$ ), Ni/Al<sub>2</sub>O<sub>3</sub> ( $= 0.34$ ) and Ni/GPL ( $= 0.19$ ). The wear profiles for various cycles are the moving mean of analysed interferometric data, for instance the interferometric wear profile of Ni/Al<sub>2</sub>O<sub>3</sub> at  $i = 10,000$  shown in red. The figures on the right in every cell represent the calculated wear depth kinetics  $h_{(i)}(x)$  at various cycles. The wear depth kinetics profiles were developed by using the incremental expression taken from [41].

With increasing fretting cycles the normalised wear depth kinetics profiles decrease significantly. It can be seen that the highest decreasing rate profile was observed for the case of Ni/ZrO<sub>2</sub> followed by Ni/SiC, Ni/Al<sub>2</sub>O<sub>3</sub> and Ni/GPL. For instance, at  $i = 8000^{\text{th}}$  cycle, Ni/ZrO<sub>2</sub> showed smallest normalised wear depth kinetics (0.09) compared to Ni/SiC (0.1), Ni/Al<sub>2</sub>O<sub>3</sub> (0.19) and Ni/GPL (0.21). Another worth noting point is that the profile grows in a manner such that it initiates as an elliptical and then decreases to hertzian and lastly becomes a quasi-flat shaped. The contact edges for  $i \geq 8000^{\text{th}}$  cycle (quasi-flat) indicate the type of wear deformation for instance severe micro-cutting in Ni/ZrO<sub>2</sub> and less severe micro-cutting in Ni/SiC is indicated by almost full flat distribution with heightened contact edges while micro-delamination and micro-ploughing in Ni/Al<sub>2</sub>O<sub>3</sub> and Ni/GPL respectively is indicated by less heightened contact edges.

Table 4. The wear depth profiles (left figures in each cell); the calculated wear depth kinetics profiles (right figures in each cell).



### 3. A 2-D Predictive Model

The well-known Archard equation is a simple model to describe reciprocating adhesive wear with the available wear volume  $V$ , Archard factor  $W$ , the hardness  $H$  of the coating and the dimensionless wear rate coefficient  $K$  [42, 47].

$$V = K \cdot \frac{W}{H} \quad 3$$

In this section, novel mechano-wear equations for the nanocomposite coating have been developed. This model is based on the ‘Archard factor density concept’ presented by Khan-Nazir [41]. The model shows the wear depth  $h(x)$  ( $\mu\text{m}$ ) in relation with the Archard factor density  $W(x)$  ( $\text{N m}/\mu\text{m}^2$ ) at different fretting cycles ‘ $i$ ’ along the sliding interface  $x$ . Fig. 12 shows their profile at various cycles which starts as hertzian and then reduces to elliptical and finally converges as quasi-flat shaped (as previously shown in Table 4).

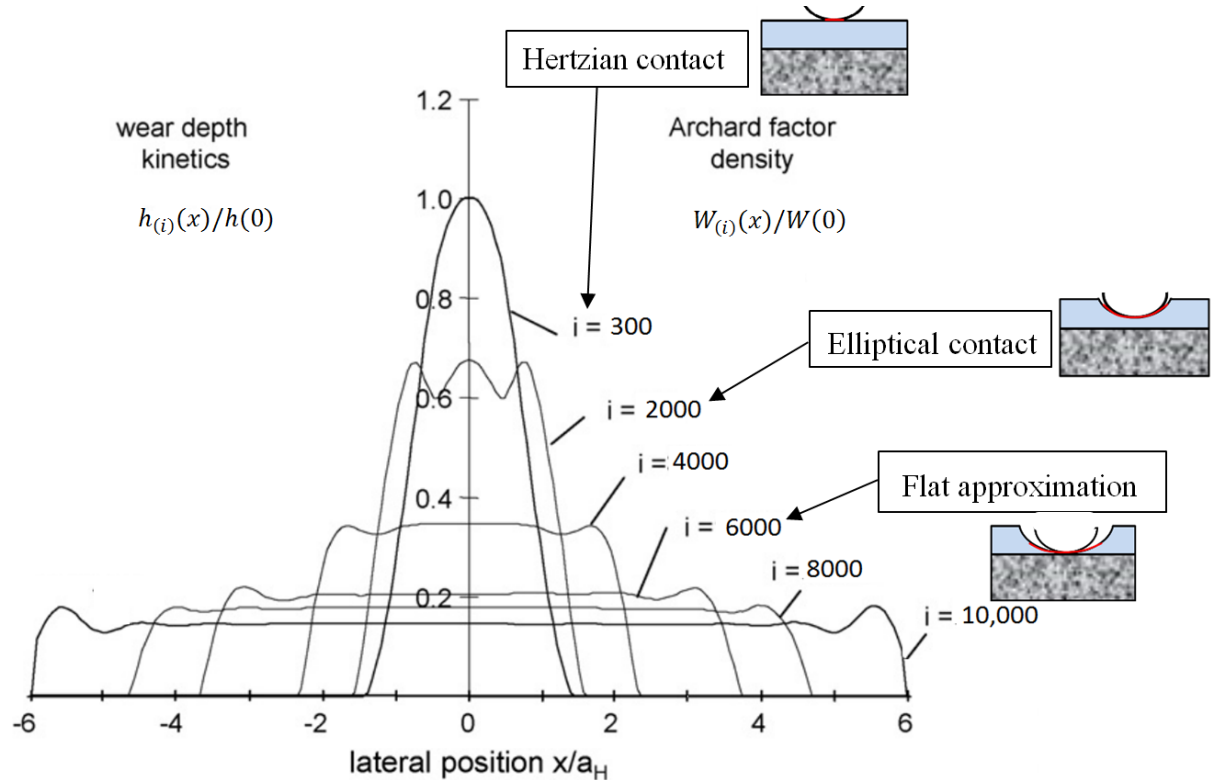


Figure 12. The profile growth of normalised wear depth kinetics and Archard factor density starting as Hertzian and reducing to elliptical and finally converging as quasi-flat shaped at different  $i^{\text{th}}$  fretting cycles [48].

The model predicts the accumulated Archard factor density  $\sum W(0)$  by relating  $h(0)$  at  $x/a_H = 0$  with respect to corresponding wear depth kinetics  $h_{(i)}(x)$  (discussed in section 2.3.3 and Table 4). Three hypothesis (Hertzian-Elliptical-Flat shown in Fig. 12) have been taken to numerically calculate the value of  $W$  subject to condition when the relative sliding ‘ $\delta_g$ ’ stays less than the contact radius ‘ $a$ ’ (i.e.  $\delta_g < a$ ) for a constant linear normal force  $P_L$ .

It is worth noting that the mathematical analysis assumes: gross sliding and half-space contact configurations.

#### 3.1. Hertzian, Elliptical and Flat contact formulation

Initially, Hertzian approximation assumes that no wear has taken place at the interface and both contact dimension and pressure are retained constant. During the  $i^{\text{th}}$  cycle the dissipated Archard factor density at  $x = 0$ , which is the interface centre, is constant and is given as [41]:

$$W_{H(i)}(0) = 2p_{OH}\delta g_{(i)} \left( \left( 1 - \left( \frac{\delta g_{(i)}}{a_H} \right)^2 \right)^{\frac{1}{2}} + \arcsin \left( \frac{\delta g_{(i)}}{a_H} \right) \right) \quad 4$$

It was shown that wear results in major change at the interface along with the extension of contact region. Therefore the next hypothesis considers the elliptical distribution of the Archard factor density with extended contact area  $a_{(i)}$  and is given as [41]:

$$W_{E(i)}(0) = 2p_{OE}\delta g_{(i)} \left( \left( 1 - \left( \frac{\delta g_{(i)}}{a_{(i)}} \right)^2 \right)^{\frac{1}{2}} + \arcsin \left( \frac{\delta g_{(i)}}{a_{(i)}} \right) \right) \quad 5$$

Where  $p_{OH}$  and  $p_{OE}$  respectively, are the maximum Hertzian and maximum elliptical pressures. The  $a_H$  and  $a_{(i)}$  respectively are the partial widths of the Hertzian and elliptical contacts respectively.

It has been shown that the Archard factor density becomes quasi-flat shaped beyond some number of cycles given as [41]:

$$W_{F(i)}(0) = \frac{1}{2a_{(i)} + \delta g_{(i)}} \quad 6$$

Here, it is assumed that  $p_{OH} = p_{OE}$  and  $a_H = a_{(i)}$  therefore,

$$p_{OH} = p_{OE} = \frac{2P_L}{\pi a_H} \quad \text{and} \quad a_H = a_{(i)} = \frac{4P_LR}{\pi E^*} = \frac{4RV}{\pi} \quad 7$$

Where  $R$  is the radius of the ball. The  $P_L$  is the linear normal force and  $E^*$  is the equivalent Young modulus given as.

$$P_L = \frac{P}{L} \quad \text{and} \quad \frac{1}{E^*} = \frac{1-v_1^2}{E_1} + \frac{1-v_2^2}{E_2} \quad 8$$

Where  $P$  is the normal force applied,  $L$  is the contact length of coating and ball,  $E_1$ ,  $E_2$  and  $v_1$ ,  $v_2$  are the Young's moduli and Poisson ratios of the coating (subscript 1) and the ball (subscript 2) respectively.

### 3.2. Mechanics formulation

It is worth noting that the coating's Young's modulus  $E_1$  (eq. 8) is linked with the extrinsic residual stress  $\sigma_c$  (Fig. 13) at the fretting scar's centre and nano particle size (diameter)  $D_p$  of coating as [41, 49, 50].

$$D_p = \left[ \frac{\left[ 1 - \left( \gamma_s e^{-\frac{\sigma_c(0)}{E_1}} \right) \right]^2 k_s}{\left[ \gamma_s e^{-\frac{\sigma_c(0)}{E_1}} \right]^3} \right]^{\frac{1}{2}} \quad 9$$

Where  $k_s = \beta P_s^m$  is the surface permeability of coating with  $\beta$  and  $m$  are the material properties;  $\gamma_s$  is the stress sensitivity coefficient [51]. The extrinsic residual stress  $\sigma_c(0)$  in the coating at the interface develops when the coating substrate system with coefficient of thermal mismatch encounters the variation in temperature  $\Delta T$  from the deposition temperature during wear testing.

A classical solution to calculate the extrinsic residual stress in a coating-substrate system at the centre of the interface is given as [41, 52].



$$\sigma_c(0) = E_1 \left[ \frac{(E_3 \alpha_s s + E_1 \alpha_c h_c(0)) \Delta T}{(E_3 s + E_1 h_c(0))} + x - t_b \left( \frac{E_3 s^2 (2s + 3t_b) + E_1 h_c^2 (2h_c(0) - 3t_b)}{3 \left[ E_3 s^2 \left( \frac{(E_3 \alpha_s s + E_1 \alpha_c h_c(0)) \Delta T}{(E_3 s + E_1 h_c(0))} - \alpha_s \Delta T \right) - E_1 h_c^2 \left( \frac{(E_3 \alpha_s s + E_1 \alpha_c h_c(0)) \Delta T}{(E_3 s + E_1 h_c(0))} - \alpha_c \Delta T \right) \right]} \right) - \alpha_c \Delta T \right] \quad 10$$

Where,  $E_3$  is the elastic modulus of substrate;  $\alpha_c$  and  $\alpha_s$  are the coefficient of thermal mismatch of coating and substrate respectively;  $h_c(0)$  is the coating thickness at  $x = 0$ ;  $t_b = \frac{-E_3 s^2 + E_1 h_c^2(0)}{2(E_3 s + E_1 h_c(0))}$  indicates the bending axis location [53],

The average maximum grain size  $D$  can be calculated by using eq. 9 as [41, 54].

$$D = \frac{D_p}{2} (\bar{U})^{\frac{1}{2}} + D_p \quad 11$$

Where  $\bar{U}$  is the grain creep sensitivity coefficient [41]. Post-deformation grain size is referred to as average maximum grain size while pre-deformation grain size at the time of deposition is referred to as deposit grain size  $D_p$ . Eq. 11 is based on the assumption that the particles during wear deformation are inseparable from the grain boundaries.

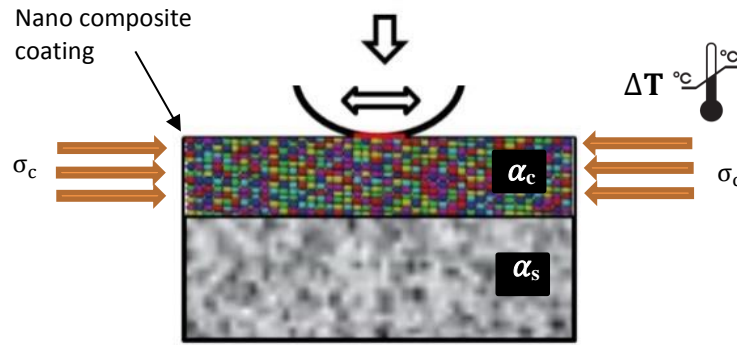


Figure 13. The schematic shows the evolution of residual stresses due to thermal mismatch during the wear process.

The former expressions eq. 4, 5 and 6 represent the local wear depth analysis corresponding to local Archard factor density  $W$  ( $N\ m/\mu m^2$ ). It is worth noting that the global wear analysis and the local wear analysis both are directed by the same physical dimensions. In the case of analysis for global wear the Archard factor  $W$  ( $N\ m$ ) is linked with entire wear volume  $V$  ( $m^3$ ) of scar while for the case of analysis for local wear the Archard factor density  $W$  ( $N\ m/\mu m^2$ ) is only linked with the wear depth  $h(x)$  ( $m$ ) of scar. Therefore for addressing the global wear analysis, the former expression eq. 4, 5 and 6 can be modified for expressing the local loading factor in relation with the global Archard factor  $W$ .

$$W_{H(i)=E(i)}(0) = W_{H(i)}(0) = W_{E(i)}(0) = \frac{W_{(i)}}{\pi \delta g_{(i)} L} \left( \frac{\delta g_{(i)}}{a_{(i)}} \left( 1 - \left( \frac{\delta g_{(i)}}{a_{(i)}} \right)^2 \right)^{\frac{1}{2}} + \arcsin \left( \frac{\delta g_{(i)}}{a_{(i)}} \right) \right) \quad 12$$

$$W_{F(i)}(0) = \frac{W_{(i)}}{(2a_{(i)} + \delta g_{(i)}) L} = \frac{W_{(i)}}{2a_{(i)} L \left( 1 + \frac{\delta g_{(i)}}{2a_{(i)}} \right)} \quad 13$$

Next by adding Hertzian/elliptical and flat distribution formulations, a dual equation to model the global Archard factor density evolution from Hertzian /elliptical (eq. 12) to quasi-flat formulation (eq. 13) is given as [41].

$$\begin{aligned} \sum W(0) = \sum W_{H(i)=E(i)}(0) + W_{F(i)}(0) = \sum_{i=1}^{i_{ft}} \left[ \frac{W_{(i)}}{\pi \delta g_{(i)} L} \left( e_{(i)} \left( 1 - (e_{(i)})^2 \right)^{\frac{1}{2}} + \arcsin(e_{(i)}) \right) \right] + \\ \sum_{i=i_{ft}}^N \left[ \frac{W_{(i)}}{2a_{(i)} L \left( 1 + \frac{e_{(i)}}{2} \right)} \right] \end{aligned} \quad 14$$

Less than a threshold wear  $a_{ft}$  and cycle  $i_{ft}$ , the Archard factor density is given by Hertzian/elliptical distribution (eq. 12), however above the threshold value of wear and cycle, the flat distribution is considered (eq.13).

### 3.3. Prediction of the wear volume, wear rate and friction coefficient

The above equation (eq. 14) is used for analysing the ball/coating contact. For this, accumulated  $W$  (N m/  $\mu\text{m}^2$ ) is compared with the maximum wear depth  $h(x)$  (m). This analysis includes equating the evolution of contact radius. Assuming that the ball is spherical in shape, the contact length  $S_{(i)}$  and the wear volume  $V_{(i)}$  are given as (Fig. 14).

$$S = 2\pi R h \quad \text{and} \quad V = \frac{1}{3} \pi h^2 (3R - h) \quad 15$$

Where,  $V$  is the wear volume in  $\mu\text{m}^3$ . Solving the above equation leads to:

$$V = \frac{1}{3} \frac{\pi S^2}{(2\pi R)^2} R \left( 3 - \frac{h}{R} \right) \quad 16$$

Therefore with  $h \ll R$  it is deduced that:

$$V = \frac{1}{4\pi R} S^2 \quad 17$$

Combined with  $S = \pi a^2$  modifies to:

$$a = \left( \frac{4R}{\pi} \right)^{\frac{1}{4}} V^{\frac{1}{4}} \quad 18$$

The wear volume relates to  $\sum W$  as [41].

$$V = K_v \sum W \quad 19$$

Where  $\sum W$  is the accumulated Archard factor (N m).

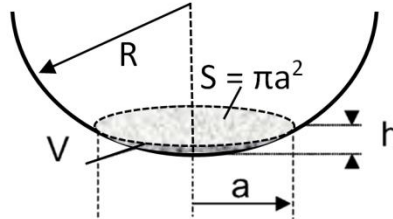


Figure 14. Schematic of steel ball (cross-section) in contact with the coating.

Lastly, the contact radius as a function of the Archard loading factor is written as:

$$a = \left( \frac{4RK_v}{\pi} \right)^{\frac{1}{4}} \sum W^{\frac{1}{4}} \quad 20$$

The above equation only addresses the worn interface, in order to add the contribution of initial Hertzian contact (when wear has not actually initiated) eq. 20 is finalised by addition of the preliminary Hertzian component  $a_H$ . At the  $i^{\text{th}}$  cycle, the contact radius  $a_{(i)}$  is written as.

$$a_{(i)} = A \sum W_{(i)}^{\frac{1}{4}} + a_H \quad 21$$

Where coefficient  $A$  includes the wear rate  $K_v$  and the contact geometry  $R$ .

The wear rate can be quantified from eq. 19 by relating the wear volume (V) (eq. 17) with Archard factor ( $\Sigma W$ ) (eq. 14). The wear rate coefficient is then given by.

$$K_v = \frac{V}{\Sigma W} \quad 22$$

The average friction response can be calculated as [55-61].

$$\mu = \frac{E_d}{4P_L \delta_g} \quad 23$$

Where  $E_d$  is the energy dissipated which can be related with the wear volume V as [55-61].

$$E_d = \frac{V - \beta}{\alpha} \quad 24$$

Where  $\alpha$  is the energy wear coefficient ( $\mu\text{m}^3/\text{J}$ ), and  $\beta$  is the residual value ( $\mu\text{m}^3$ ). For reliable friction coefficient results both  $\alpha$  and  $\beta$  must be set-up very-accurately either through experimental results or repeated simulations. In present model these have been calculated from experimental data as-well-as repeated simulations.

#### 4. Modelling Results and Discussion

MD (Molecular Dynamic) simulations were conducted to study the intrinsic atomic level wear and friction properties of nanocrystalline coatings. MD simulations for Ni/ $\text{Al}_2\text{O}_3$ , Ni/SiC, Ni/ $\text{ZrO}_2$  and Ni/GPL nanocomposite coatings FCC crystals were performed with LAMMPS algorithm [62, 63]. Embedded-atom technique was utilised to simulate the crystals [64, 65]. All simulations were conducted in a molecular statics framework and implemented by using the conjugate gradient method [65].

The simulation assumes the nanocomposite coating specimen made of Ni-matrix and the ball made of steel. The x-axis lies horizontal to the coating surface while y-axis lies perpendicular to the coating surface. The analysis of atoms along the xy plane for the Ni based composites is performed. The 1600 atoms are arranged in 80 atoms/layer in x dimension in a total 20 layers along y direction. The sample surface is assumed to be well-defined at atomic level.

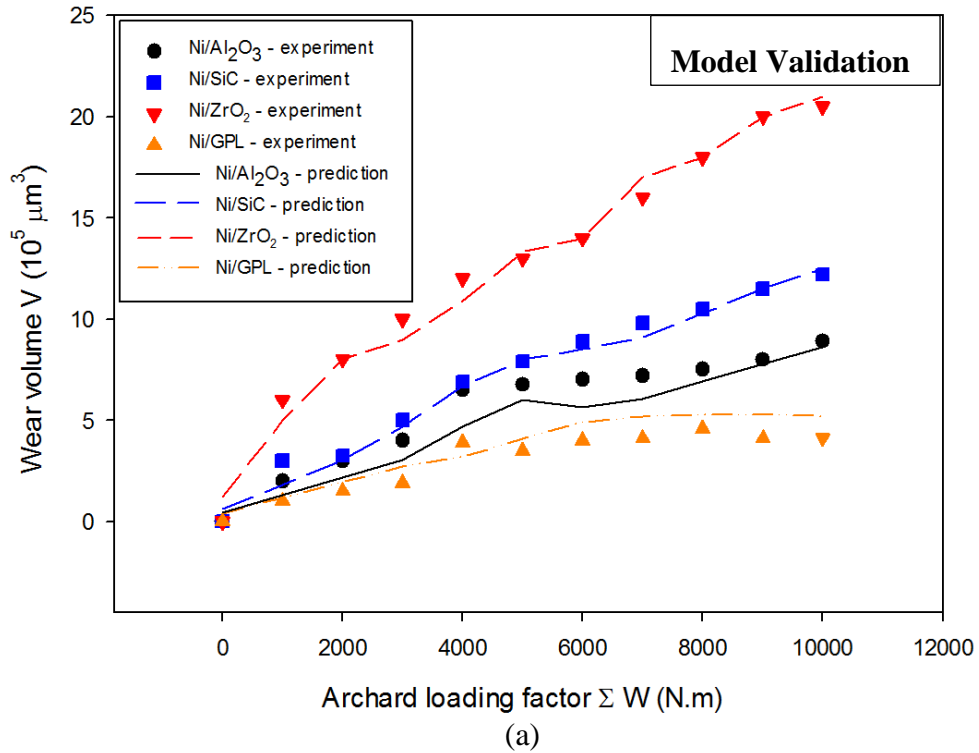
By using law of minimum potential energy, the layers of atoms in Ni matrix are attained at the lowest thermodynamic temperature (i.e. 0 K) for reference in order to arrange the atomic layers by considering thermal expansion and mean velocity vectors at room temperature. The velocity calculations are performed by using Newton's equations of motion and velocity scaling is performed until the system stabilises completely. This results in the formation of the atomic layer model at room temperature. The average distance between two adjacent atoms is about 0.21 nm which is normal inter-atomic distance in Ni matrix compounds. In current study, wear and friction processes without plastic deformation are studied. MD simulations delivered the material parameters values:  $\alpha$ ,  $\beta$ , m and  $\rho$ . Additional material parameters were taken from references stated in Table 1 and were experimentally confirmed. These parameters mentioned in Table 5 are based on assumption that the thicknesses of all studied coatings were 10  $\mu\text{m}$  (from experiment).

Table 5. Parametric values generated by using MD simulations

Materials	$\nu$	E (GPa)	H (HV)	CTE ( $\times 10^{-6}/\text{K}$ )	$\alpha$ ( $\mu\text{m}^3/\text{J}$ )	$\beta$ ( $\mu\text{m}^3$ )	m	$\rho$	$D_o$ (nm)
Ni/ $\text{Al}_2\text{O}_3$	0.28 [66]	275 [12]	~452	14.2 [66]	0.21	0.1	0.1	1.8	16.08
Ni/SiC	0.24 [66]	310 [12]	~410	15 [67]	1.7	0.8	0.8	2.9	18.65
Ni/ $\text{ZrO}_2$	0.21 [68]	220 [12]	~390	15.2 [67]	2.3	0.4	0.4	3.5	19.68

<b>Ni/GPL</b>	0.19 [69]	240 [70]	~480	13.3 [67]	1.1	1.5	1.5	0.9	11.21
<b>Steel ball</b>	0.3 [71]	210 [71]	740	11.7 [72]	-	-	-	-	-

The simulations for wear volumes and friction coefficients for all coatings were performed by using the parametric values in Table 5 in to the mechano-wear equations as shown in Fig. 15. The predicted wear volumes and friction coefficients were validated by comparison with the experimental results to validate the model reliability as shown in Fig. 15 (a) and (b). Both the predicted and experimental results were in close relation except few data points where model slightly over predicted the predictions, making some points in both graphs to deviate from the experimental data. For validation, both wear volumes and friction coefficients were plotted as a function of Archard loading factor. As anticipated, the predicted wear volumes increased linearly while friction coefficients stabilised following a preliminary increase as a function of Archard loading factor, same as was observed experimentally.





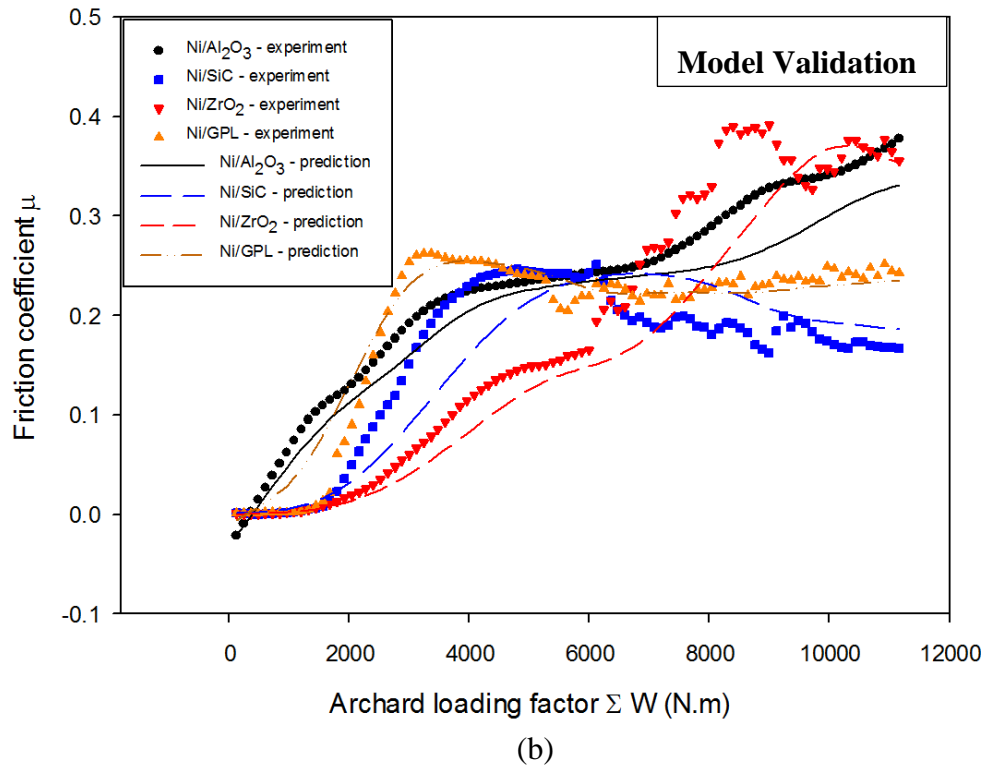


Figure 15. The comparison of experimental and predicted (a) wear volumes and (b) friction coefficients results for validation of the model reliability.

Predicted wear volumes and friction coefficients with varying percentage porosity for Ni/Al<sub>2</sub>O<sub>3</sub>, Ni/SiC, Ni/ZrO<sub>2</sub> and Ni/GPL are shown in Fig. 16 (a) and (b). It can be seen from Fig. 16 (a) that the porosity directly influences the overall wear volume such that 21, 16, 14 and 9 % rise in overall wear volumes of Ni/ZrO<sub>2</sub>, Ni/SiC, Ni/Al<sub>2</sub>O<sub>3</sub> and Ni/GPL respectively was observed when the porosity of all coatings was increased from 5% to 25%. The Ni/ZrO<sub>2</sub> had the highest percentage rise in wear volume (21%) while Ni/GPL had the smallest rise in wear volume (9%). This is because Ni/ZrO<sub>2</sub> has the highest deposit grain size  $D_0$  (19.68 nm) [Table 5]. When the porosity of nanocomposite coatings with larger deposit grain size increases, the grain boundaries become more disordered compared with the coatings which have smaller deposit grain size [73]. These largely disordered grain boundaries in a coating result in large wear rate. Based on this it can be seen that the largest wear volume was found in Ni/ZrO<sub>2</sub> (21%) which had largest deposit grain size followed by Ni/SiC (16%), Ni/Al<sub>2</sub>O<sub>3</sub> (14%) and Ni/GPL (9%).

Fig. 16 (b) shows the percentage rise in friction coefficient when the porosity was increased from 5% to 25%. The plots reveal that Ni/ZrO<sub>2</sub> showed the highest percentage rise (31%) in friction coefficient followed by Ni/SiC (14%), Ni/Al<sub>2</sub>O<sub>3</sub> (13%) Ni/GPL (12%). Based on this it can be inferred that friction coefficients of all coatings are influenced by deposit grain size, as also in the case of wear volumes. The Ni/ZrO<sub>2</sub>, which had the highest deposit grain size (19.68 nm) showed the largest percentage rise in fiction coefficient (31%) while Ni/GPL with the minimum deposit grain size (11.21 nm) showed the smallest percentage rise in fiction coefficient (12%).

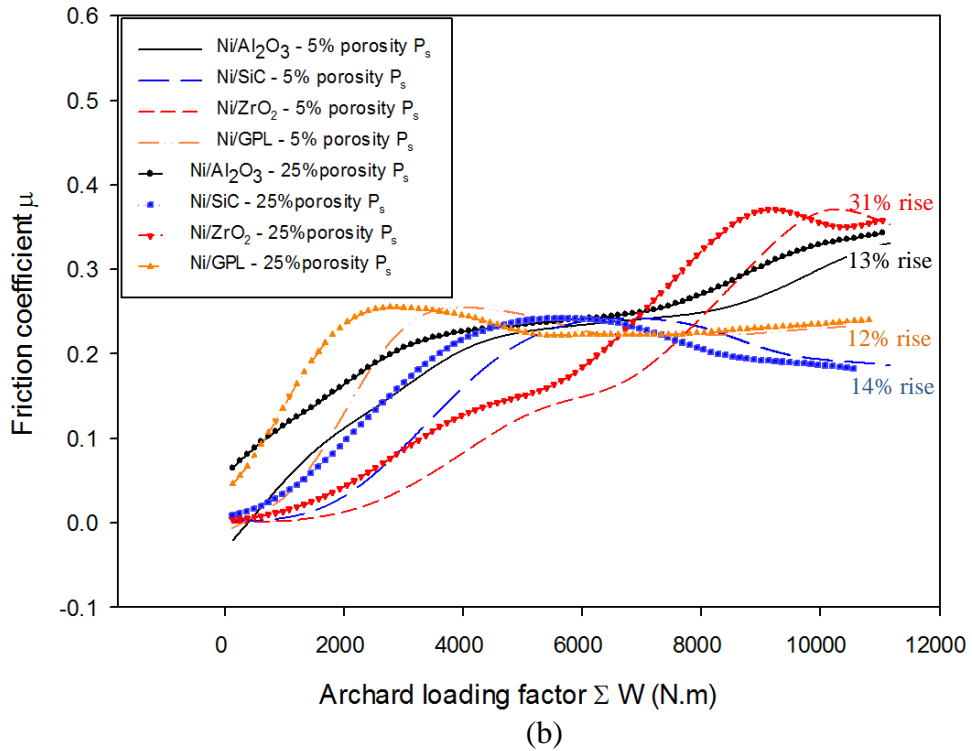
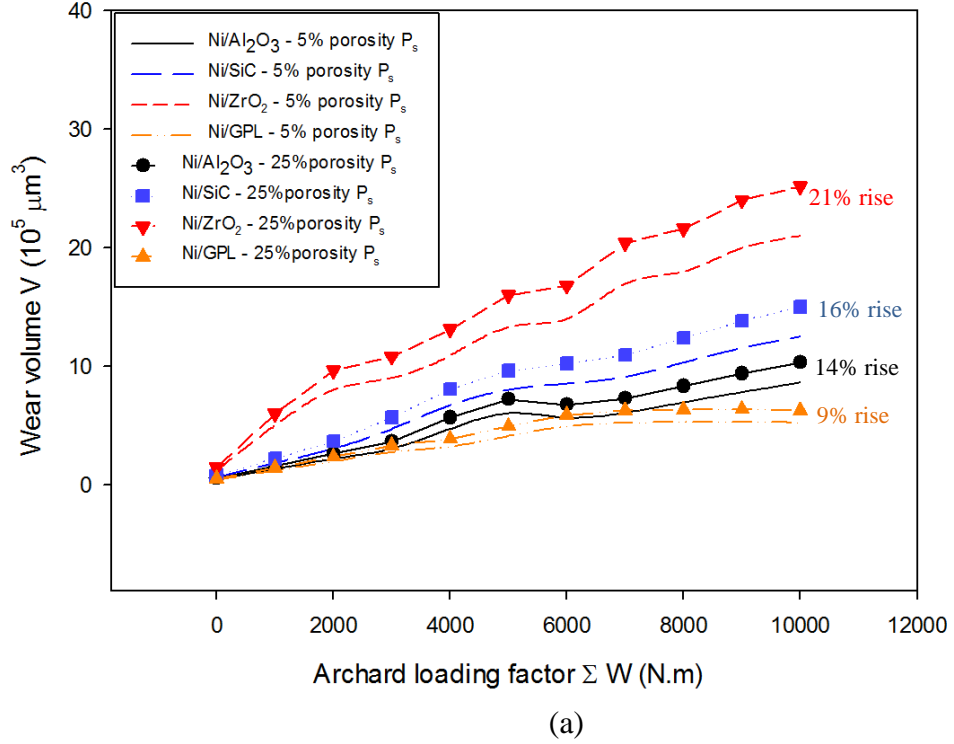
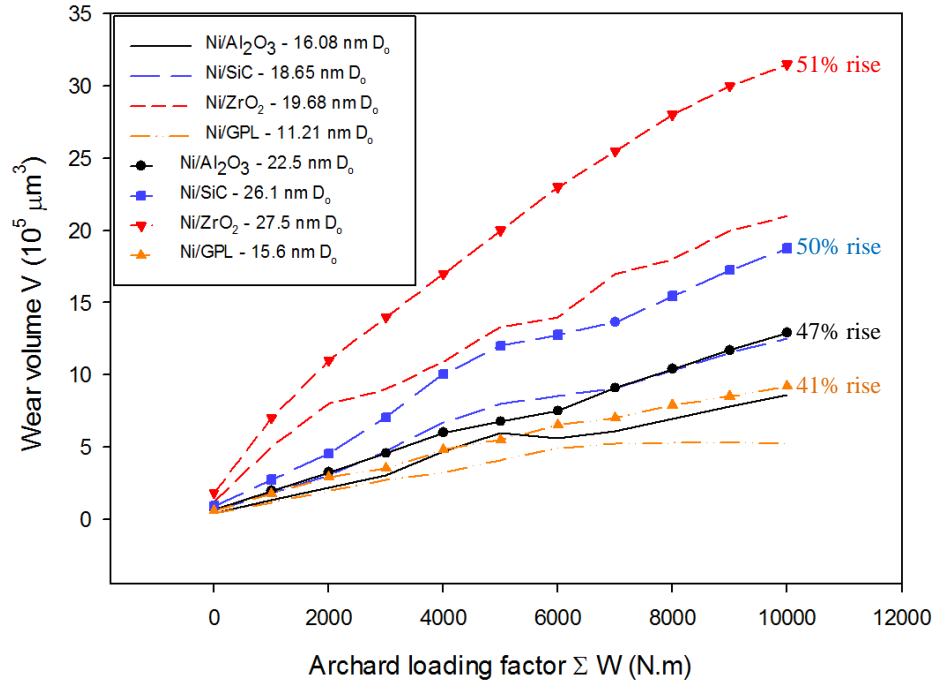


Figure 16. The predicted (a) wear volumes and (b) friction coefficients for various percentage porosity values with respect to Archard loading factor.

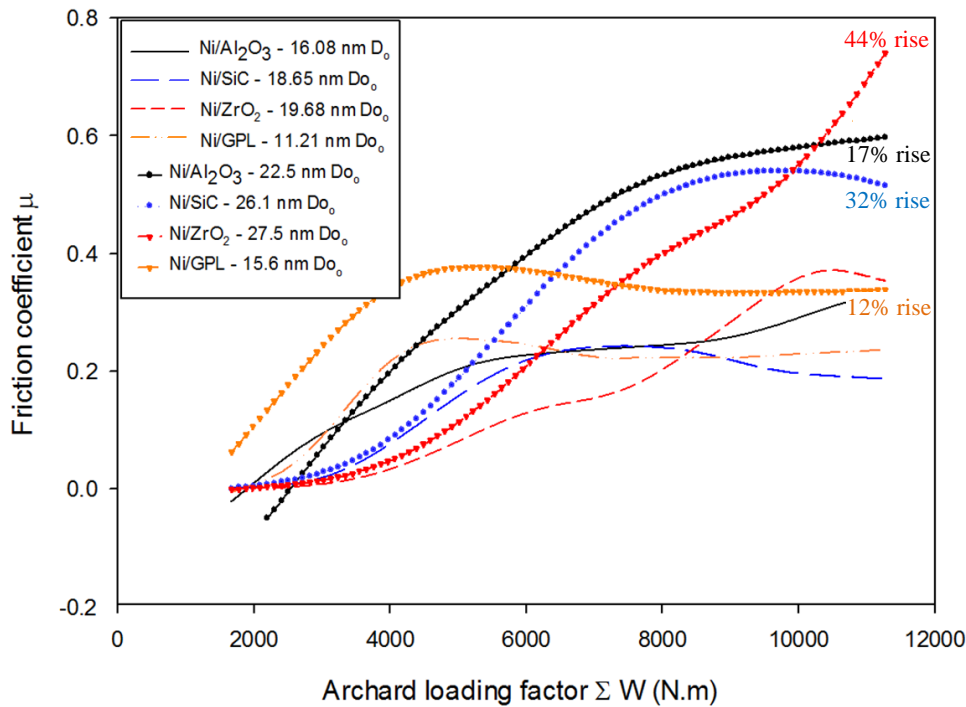
Fig. 17 (a) plots the effect of increase in deposit grain size on the wear volume of all nanocomposite coatings. It is observed that with the increase in grain size by 40% for all the coatings, a significant increase in the wear volume of all the coatings was observed. Large deposit grain size results in significant cracking which accelerates grain loss during fretting cycles. Contrarily, small deposit grain size with finely distributed network in the Ni-matrix exhibit far-better inter-granular bonding avoiding grain loss.

This is the reason that Ni/Al<sub>2</sub>O<sub>3</sub>, Ni/SiC, Ni/ZrO<sub>2</sub> and Ni/GPL coatings showed very high percentage rise in wear volume with 40% rise in deposit grain size. It is noteworthy that Ni/ZrO<sub>2</sub> showed the highest percentage (51%) rise in wear volume followed by Ni/SiC (50%), Ni/Al<sub>2</sub>O<sub>3</sub> (47%) and Ni/GPL (41%). The reason for the lowest percentage rise in wear volume of Ni/GPL with increased deposit grain size is linked with the fine grain compared with the other coatings. The fine texture does not account for much rise in wear volume.

The predictions in Fig. 17 (b) showed that the friction coefficient increased with the 40% increase in deposit grain size. The highest percentage rise was found for Ni/ZrO<sub>2</sub> (44%) followed by Ni/SiC (32%), Ni/Al<sub>2</sub>O<sub>3</sub> (17%) and Ni/GPL (12%). The reason for lowest percentage rise in Ni/GPL is linked to the lowest surface roughness due to fine grains compared to other coatings, as discussed previously.



(a)

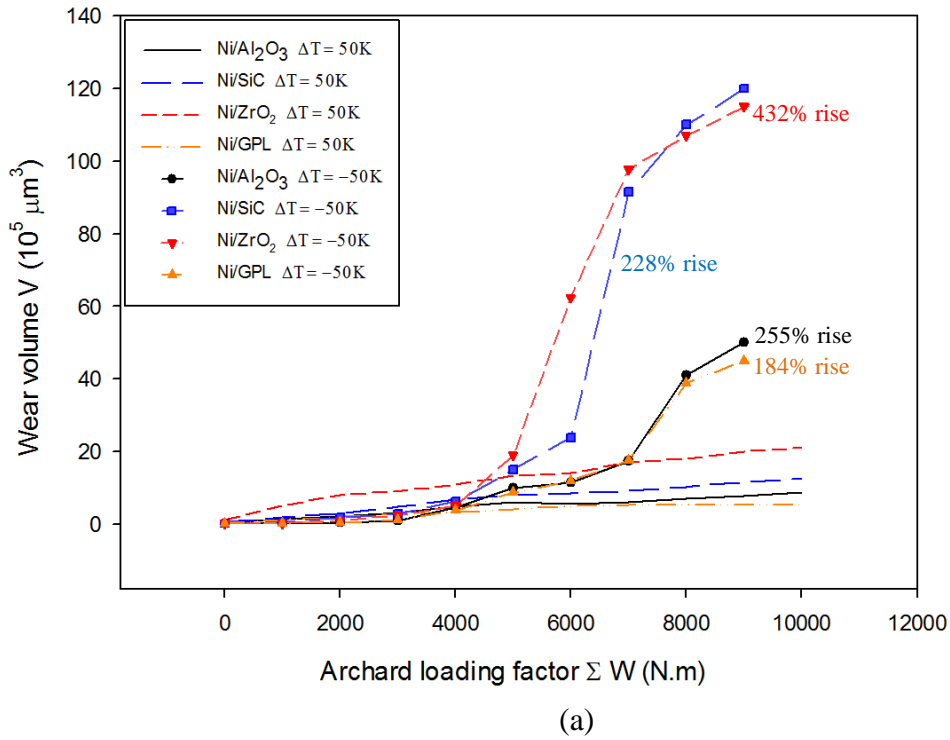


(b)

Figure 17. The predicted (a) wear volumes and (b) friction coefficients for various deposit grain sizes with respect to Archard loading factor.

Fig. 18 (a) plots the effects of temperature change from deposition temperature  $\Delta T$  on the wear volume of all the nanocomposite coatings. The change  $\Delta T$  results in extrinsic residual stress due to the coating/substrate thermal mismatch coefficient [74]. The fretting cycles under this behaviour gives higher wear volume. The Ni composite coatings ( $\alpha_c = 13 - 17 \times 10^{-6} \text{ K}^{-1}$ ) offer higher thermal mismatch coefficient compared to steel substrate ( $\alpha_s = 12.0 \times 10^{-6} \text{ K}^{-1}$ ) [72], therefore negative temperature change ( $\Delta T = -50\text{K}$ ) results in tensile residual stress in the coating whereas the positive temperature change ( $\Delta T = 50\text{K}$ ) results in compressive residual stress [75]. The change in  $\Delta T$  from  $50\text{K}$  to  $-50\text{K}$  after  $\sum W > 4000$  becomes significant and results in large rise in the wear volume. It can be seen that Ni/ZrO<sub>2</sub> showed the highest percentage rise (432%) in wear volume followed by Ni/SiC (228%), Ni/Al<sub>2</sub>O<sub>3</sub> (255%) and Ni/GPL (184%). The reason for significant change in wear volume of all the coatings is that under tensile conditions the possibility of crack initiation and propagation in the surface becomes very high. Another worth noting point is exponential rise when  $\sum W > 4000$ , because after this point the coating thickness  $h_c$  at the centre of contact becomes very thin. Thin coatings after constant worn-out develop high residual stress [74].

Fig. 18 (b) shows the variation in the friction coefficients of all the coatings with the change in  $\Delta T$ . The change in  $\Delta T$  from  $50\text{K}$  to  $-50\text{K}$  resulted in significant percentage increase in the friction coefficient. The highest percentage rise was found for Ni/ZrO<sub>2</sub> (189%) followed by Ni/SiC (185%), Ni/Al<sub>2</sub>O<sub>3</sub> (180%) and Ni/GPL (176%). The variation in residual stress from compressive to tensile corresponding to  $\Delta T$  change resulted in high cracking and wear debris offering high friction coefficient.





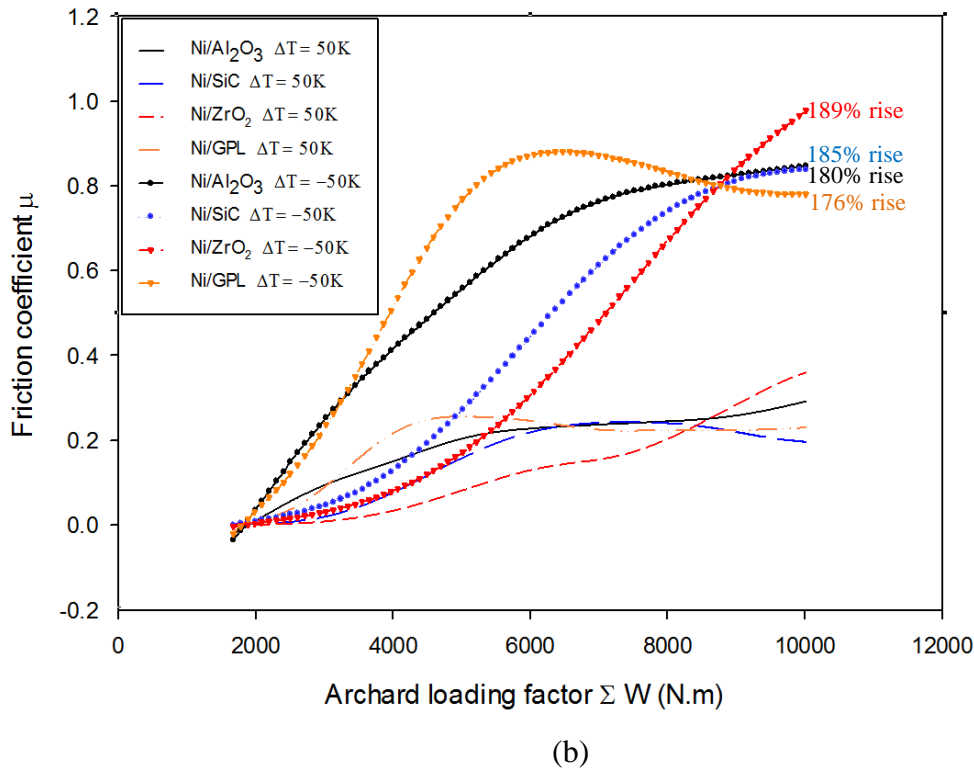


Figure 18. The predicted (a) wear volumes and (b) friction coefficients as a function of temperature change  $\Delta T$  with respect to Archard loading factor.

## 5. Conclusions

In this work, the wear performance of nanocomposite coatings: Ni/Al<sub>2</sub>O<sub>3</sub>, Ni/SiC, Ni/ZrO<sub>2</sub> and Ni/Graphene (GPL) was analysed by comprehensive experimental study which was then utilised to develop novel mechano-wear predictive equations 19, 22, 23 and 24 which are able to predict the wear reliability of nanocomposite coatings.

This study concludes the following points:

- Presented study concludes that Ni/ZrO<sub>2</sub> composite exhibits maximum wear rate followed by Ni/SiC and Ni/Al<sub>2</sub>O<sub>3</sub> and Ni/GPL respectively. This was also assured by “U-shaped” wear profiles for maximum wear depths (Table 4).
- The wear rates – hardness trend for all nanocomposite coatings subject of this study showed a linear decrease of wear rate with increasing coating hardness. It was revealed that Ni/ZrO<sub>2</sub> which had the least hardness, demonstrated the highest wear rate while Ni/GPL which had the highest hardness showed the lowest wear rate. This behaviour showed that for nanocomposite coatings wear rate is inversely related to hardness.
- Likewise, the friction coefficients – hardness trend showed no specific relation between the two, rather friction coefficient was more influenced by wear debris instead of hardness. It was shown that Ni/Al<sub>2</sub>O<sub>3</sub> revealed the highest friction coefficient due to wear debris as a result of micro-delamination followed by Ni/ZrO<sub>2</sub>, Ni/SiC both showing micro-cutting and Ni/GPL showing micro-ploughing.
- The “U-shaped” wear profiles were utilised for calculating the wear depth kinetics profiles for all the nanocomposite coatings. The evaluation of these profiles showed a decreasing behaviour starting from Hertzian to elliptical and finally converging to quasi-flat shaped with increasing fretting cycles. The results revealed the highest decreasing rate profiles were observed for Ni/ZrO<sub>2</sub> followed by Ni/SiC, Ni/Al<sub>2</sub>O<sub>3</sub> and Ni/GPL.
- The geometric formulations for Hertzian, elliptical and quasi-flat wear depth kinetics profiles were used to develop a 2-D mechano-wear model (equations 19, 22, 23 and 24) for analysing the energy distribution

corresponding to these profiles. The model was used to study the influences of various mechanical parameters on the wear behaviour of nanocomposite coatings.

- The experimental results were used to validate the model predictions showing that the wear rates and friction coefficients of all nano-coatings of concern increased with increasing grain size due to increasing eigenstress, porosity and thermal mismatch of nano-coatings.

## Acknowledgement

The authors would like to acknowledge Schaeffler Technologies AG & Co. KG, 91074 Herzogenaurach, Germany for their financial and in-kind support for conducting this research. Authors would also like to thank Paola Barbuto, Stephen Fordham and Dean Bernard at SciTech Bournemouth University for supporting surface analyses and measurement techniques.

## Reference

- [1] P. H. C. Camargo, K. G. Satyanarayana, and F. Wypych, "Nanocomposites: synthesis, structure, properties and new application opportunities," *Materials Research*, vol. 12, pp. 1-39, 2009.
- [2] P. Jost, "Economic impact of tribology," *Proc Mechanical Failures Prevention Group*, pp. 117-139, 1976.
- [3] M. A. Meyers, A. Mishra, and D. J. Benson, "Mechanical properties of nanocrystalline materials," *Progress in materials science*, vol. 51, pp. 427-556, 2006.
- [4] K. Kumar, H. Van Swygenhoven, and S. Suresh, "Mechanical behavior of nanocrystalline metals and alloys," *Acta materialia*, vol. 51, pp. 5743-5774, 2003.
- [5] Y. Z. L. ZUO, "Materials design of microstructure in grain boundary and second phase particles," 2003.
- [6] W. Schwarzacher, "Electrodeposition: a technology for the future," *Electrochemical Society Interface*, vol. 15, pp. 32-33, 2006.
- [7] C. Low, R. Wills, and F. Walsh, "Electrodeposition of composite coatings containing nanoparticles in a metal deposit," *Surface and Coatings Technology*, vol. 201, pp. 371-383, 2006.
- [8] A. Möller and H. Hahn, "Synthesis and characterization of nanocrystalline Ni/ZrO<sub>2</sub> composite coatings," *Nanostructured Materials*, vol. 12, pp. 259-262, 1999.
- [9] A. Karimpoor, U. Erb, K. Aust, and G. Palumbo, "High strength nanocrystalline cobalt with high tensile ductility," *Scripta Materialia*, vol. 49, pp. 651-656, 2003.
- [10] P. Gyftou, M. Stroumbouli, E. Pavlatou, P. Asimidis, and N. Spyrellis, "Tribological study of Ni matrix composite coatings containing nano and micro SiC particles," *Electrochimica Acta*, vol. 50, pp. 4544-4550, 2005.
- [11] H. Gül, F. Kılıç, S. Aslan, A. Alp, and H. Akbulut, "Characteristics of electro-co-deposited Ni–Al<sub>2</sub>O<sub>3</sub> nano-particle reinforced metal matrix composite (MMC) coatings," *Wear*, vol. 267, pp. 976-990, 2009.
- [12] R. S. Bajwa, Z. Khan, V. Bakolas, and W. Braun, "Water-lubricated Ni-based composite (Ni–Al<sub>2</sub>O<sub>3</sub>, Ni–SiC and Ni–ZrO<sub>2</sub>) thin film coatings for industrial applications," *Acta Metallurgica Sinica (English Letters)*, vol. 29, pp. 8-16, 2016.
- [13] R. S. Bajwa, Z. Khan, V. Bakolas, and W. Braun, "Effect of bath ionic strength on adhesion and tribological properties of pure nickel and Ni-based nanocomposite coatings," *Journal of Adhesion Science and Technology*, vol. 30, pp. 653-665, 2016.
- [14] J. Araújo and D. Nowell, "Analysis of pad size effects in fretting fatigue using short crack arrest methodologies," *International Journal of Fatigue*, vol. 21, pp. 947-956, 1999.
- [15] M. P. Szolwinski and T. N. Farris, "Observation, analysis and prediction of fretting fatigue in 2024-T351 aluminum alloy," *Wear*, vol. 221, pp. 24-36, 1998.

- [16] D. R. Swalla, R. W. Neu, and D. L. McDowell, "Microstructural characterization of Ti-6Al-4V subjected to fretting," *TRANSACTIONS-AMERICAN SOCIETY OF MECHANICAL ENGINEERS JOURNAL OF TRIBOLOGY*, vol. 126, pp. 809-816, 2004.
- [17] C. D. Lykins, S. Mall, and V. Jain, "An evaluation of parameters for predicting fretting fatigue crack initiation," *International Journal of Fatigue*, vol. 22, pp. 703-716, 2000.
- [18] L. Qian, Q. Sun, and Z. Zhou, "Fretting wear behavior of superelastic nickel titanium shape memory alloy," *Tribology Letters*, vol. 18, pp. 463-475, 2005.
- [19] I. McColl, J. Ding, and S. Leen, "Finite element simulation and experimental validation of fretting wear," *Wear*, vol. 256, pp. 1114-1127, 2004.
- [20] M. Kalin, J. Vižintin, S. Novak, and G. Dražič, "Wear mechanisms in oil-lubricated and dry fretting of silicon nitride against bearing steel contacts," *Wear*, vol. 210, pp. 27-38, 1997.
- [21] J. Madge, S. Leen, and P. Shipway, "A combined wear and crack nucleation–propagation methodology for fretting fatigue prediction," *International Journal of Fatigue*, vol. 30, pp. 1509-1528, 2008.
- [22] T. Yue and M. Abdel Wahab, "A numerical study on the effect of debris layer on fretting wear," *Materials*, vol. 9, p. 597, 2016.
- [23] F. Cura, W. Qureshi, and A. Mura, "A methodological approach for incremental fretting wear formulation," *Tribology Letters*, vol. 64, p. 20, 2016.
- [24] M. H. Nazir, Z. A. Khan, A. Saeed, and K. Stokes, "Modeling the Effect of Residual and Diffusion-Induced Stresses on Corrosion at the Interface of Coating and Substrate," *Corrosion*, vol. 72, pp. 500-517, 2016/04/01 2015.
- [25] M. H. Nazir, Z. A. Khan, A. Saeed, and K. Stokes, "A predictive model for life assessment of automotive exhaust mufflers subject to internal corrosion failure due to exhaust gas condensation," *Engineering Failure Analysis*, vol. 63, pp. 43-60, 2016.
- [26] M. H. Nazir, Z. A. Khan, and K. Stokes, "A holistic mathematical modelling and simulation for cathodic delamination mechanism – a novel and an efficient approach," *Journal of Adhesion Science and Technology*, pp. 1-39, 2015.
- [27] M. H. Nazir, Z. Khan, and K. Stokes, "Modelling of metal-coating delamination incorporating variable environmental parameters," *Journal of Adhesion Science and Technology*, vol. 29, pp. 392-423, 2014.
- [28] M. Nazir, Z. A. Khan, and K. Stokes, "A unified mathematical modelling and simulation for cathodic blistering mechanism incorporating diffusion and fracture mechanics concepts," *Journal of Adhesion Science and Technology*, vol. 29, pp. 1200-1228, 2015.
- [29] M. H. Nazir, Z. A. Khan, and K. Stokes, "Analysing the coupled effects of compressive and diffusion induced stresses on the nucleation and propagation of circular coating blisters in the presence of micro-cracks," *Engineering Failure Analysis*, vol. 70, pp. 1-15, 2016.
- [30] M. Nazir and Z. Khan, "A review of theoretical analysis techniques for cracking and corrosive degradation of film-substrate systems," *Engineering Failure Analysis*, 2016.
- [31] R. Bajwa, Z. Khan, H. Nazir, V. Chacko, and A. Saeed, "Wear and Friction Properties of Electrodeposited Ni-Based Coatings Subject to Nano-enhanced Lubricant and Composite Coating," *Acta Metallurgica Sinica (English Letters)*, vol. 29, pp. 902-910, 2016.
- [32] M. H. Nazir and Z. Khan, "Maximising the interfacial toughness of thin coatings and substrate through optimisation of defined parameters," *International Journal of Computational Methods and Experimental Measurements*, vol. 3, pp. 316-328, 2015.
- [33] K. Kato, M. Bai, N. Umehara, and Y. Miyake, "Effect of internal stress of CNx coating on its wear in sliding friction," *Surface and Coatings Technology*, vol. 113, pp. 233-241, 1999.
- [34] J. W. Hutchinson, "Stresses and failure modes in thin films and multilayers," *Notes for a Dcamm Course. Technical University of Denmark, Lyngby*, pp. 1-45, 1996.
- [35] T. Borkar and S. P. Harimkar, "Effect of electrodeposition conditions and reinforcement content on microstructure and tribological properties of nickel composite coatings," *Surface and Coatings Technology*, vol. 205, pp. 4124-4134, 2011.

- [36] C. P. Kumar, T. Venkatesha, and R. Shabadi, "Preparation and corrosion behavior of Ni and Ni-graphene composite coatings," *Materials Research Bulletin*, vol. 48, pp. 1477-1483, 2013.
- [37] A. Jung, H. Natter, R. Hempelmann, and E. Lach, "Nanocrystalline alumina dispersed in nanocrystalline nickel: enhanced mechanical properties," *Journal of materials science*, vol. 44, pp. 2725-2735, 2009.
- [38] D. Thiemig and A. Bund, "Influence of ethanol on the electrocodeposition of Ni/Al<sub>2</sub>O<sub>3</sub> nanocomposite films," *Applied Surface Science*, vol. 255, pp. 4164-4170, 2009.
- [39] A. Li and I. Szlufarska, "How grain size controls friction and wear in nanocrystalline metals," *Physical Review B*, vol. 92, p. 075418, 2015.
- [40] C. Binder, T. Bendo, G. Hammes, A. Klein, and J. de Mello, "Effect of nature of nitride phases on sliding wear of plasma nitrided sintered iron," *Wear*, vol. 332, pp. 995-1005, 2015.
- [41] M. H. Nazir, Z. A. Khan, A. Saeed, A. Siddaiah, and P. L. Menezes, "Synergistic wear-corrosion analysis and modelling of nanocomposite coatings," *Tribology International*, vol. 121, pp. 30-44, 2018/05/01/ 2018.
- [42] J. Archard, "Contact and rubbing of flat surfaces," *Journal of Applied Physics*, vol. 24, pp. 981-988, 1953.
- [43] E. TobyáKelsey and N. H. áde Leeuw, "Atomistic simulation of dislocations, surfaces and interfaces in MgO," *Journal of the Chemical Society, Faraday Transactions*, vol. 92, pp. 433-438, 1996.
- [44] L. Huang, K. Wang, W. Wang, J. Yuan, K. Qiao, T. Yang, P. Peng, and T. Li, "Effects of grain size and texture on stress corrosion cracking of friction stir processed AZ80 magnesium alloy," *Engineering Failure Analysis*, vol. 92, pp. 392-404, 2018.
- [45] C. Ma, S. Wang, L. Wang, F. Walsh, and R. Wood, "The role of a tribofilm and wear debris in the tribological behaviour of nanocrystalline Ni-Co electrodeposits," *Wear*, vol. 306, pp. 296-303, 2013.
- [46] T. Fischer and H. Tomizawa, "Interaction of tribochemistry and microfracture in the friction and wear of silicon nitride," *Wear*, vol. 105, pp. 29-45, 1985.
- [47] J. Archard and W. Hirst, "The wear of metals under unlubricated conditions," in *Proceedings of the Royal Society of London A: Mathematical, Physical and Engineering Sciences*, 1956, pp. 397-410.
- [48] S. Fouvry, T. Liskiewicz, and C. Paulin, "A global-local wear approach to quantify the contact endurance under reciprocating-fretting sliding conditions," *Wear*, vol. 263, pp. 518-531, 2007.
- [49] P. A. Witherspoon, J. S. Wang, K. Iwai, and J. E. Gale, "Validity of cubic law for fluid flow in a deformable rock fracture," *Water resources research*, vol. 16, pp. 1016-1024, 1980.
- [50] S. Whitaker, "Flow in porous media I: A theoretical derivation of Darcy's law," *Transport in porous media*, vol. 1, pp. 3-25, 1986.
- [51] Q. Lei, W. Xiong, J. Yuang, Y. Cui, and Y.-S. Wu, "Analysis of stress sensitivity and its influence on oil production from tight reservoirs," in *Eastern Regional Meeting*, 2007.
- [52] C.-H. Hsueh, "Modeling of elastic deformation of multilayers due to residual stresses and external bending," *Journal of Applied Physics*, vol. 91, pp. 9652-9656, 2002.
- [53] F.-Z. Xuan, L.-Q. Cao, Z. Wang, and S.-T. Tu, "Mass transport in laser surface nitriding involving the effect of high temperature gradient: Simulation and experiment," *Computational Materials Science*, vol. 49, pp. 104-111, 2010.
- [54] H.-K. Seok, K.-W. Park, and J.-C. Lee, "Particle size versus grain size relation in the sprayformed Al-18Si composites," *Metals and Materials International*, vol. 15, pp. 609-613, 2009.
- [55] S. Fouvry, P. Kapsa, H. Zahouani, and L. Vincent, "Wear analysis in fretting of hard coatings through a dissipated energy concept," *Wear*, vol. 203, pp. 393-403, 1997.
- [56] S. Fouvry and P. Kapsa, "An energy description of hard coating wear mechanisms," *Surface and Coatings Technology*, vol. 138, pp. 141-148, 2001.
- [57] S. Fouvry, T. Liskiewicz, P. Kapsa, S. Hannel, and E. Sauger, "An energy description of wear mechanisms and its applications to oscillating sliding contacts," *Wear*, vol. 255, pp. 287-298, 2003.

- [58] S. Fouvry, P. Duo, and P. Perruchaut, "A quantitative approach of Ti–6Al–4V fretting damage: friction, wear and crack nucleation," *Wear*, vol. 257, pp. 916-929, 2004.
- [59] S. Fouvry, C. Paulin, and T. Liskiewicz, "Application of an energy wear approach to quantify fretting contact durability: Introduction of a wear energy capacity concept," *Tribology International*, vol. 40, pp. 1428-1440, 2007.
- [60] C. Paulin, S. Fouvry, and S. Deyber, "Wear kinetics of Ti–6Al–4V under constant and variable fretting sliding conditions," *Wear*, vol. 259, pp. 292-299, 2005.
- [61] C. Mary and S. Fouvry, "Numerical prediction of fretting contact durability using energy wear approach: Optimisation of finite-element model," *Wear*, vol. 263, pp. 444-450, 2007.
- [62] "<http://lammps.sandia.gov>".
- [63] S. Plimpton, "Fast parallel algorithms for short-range molecular dynamics," *Journal of computational physics*, vol. 117, pp. 1-19, 1995.
- [64] S. Foiles, M. Baskes, and M. Daw, "Embedded-atom-method functions for the fcc metals Cu, Ag, Au, Ni, Pd, Pt, and their alloys," *Physical Review B*, vol. 33, p. 7983, 1986.
- [65] M. Mendelev, S. Han, D. Srolovitz, G. Ackland, D. Sun, and M. Asta, "Development of new interatomic potentials appropriate for crystalline and liquid iron," *Philosophical magazine*, vol. 83, pp. 3977-3994, 2003.
- [66] R. J. Hussey and J. Wilson, *Advanced Technical Ceramics Directory and Databook*: Springer Science & Business Media, 2012.
- [67] O. Sigmund and S. Torquato, "Composites with extremal thermal expansion coefficients," *Applied Physics Letters*, vol. 69, pp. 3203-3205, 1996.
- [68] S. Gadag, G. Subbarayan, and W. Barker, "Thermo-elastic properties of dense YSZ and porous Ni-ZrO<sub>2</sub> monolithic and isotropic materials," *Journal of materials science*, vol. 41, pp. 1221-1232, 2006.
- [69] A. Politano and G. Chiarello, "Probing the Young's modulus and Poisson's ratio in graphene/metal interfaces and graphite: a comparative study," *Nano Research*, vol. 8, pp. 1847-1856, 2015.
- [70] Z. Ren, N. Meng, K. Shehzad, Y. Xu, S. Qu, B. Yu, and J. Luo, "Mechanical properties of nickel-graphene composites synthesized by electrochemical deposition," *Nanotechnology*, vol. 26, p. 065706, 2015.
- [71] P. D. Harvey, *Engineering properties of steel*: Asm Intl, 1982.
- [72] D. R. Lide, "CRC handbook of chemistry and physics," *12J204*, 1947.
- [73] A. Sinha and Z. Farhat, "A study of porosity effect on tribological behavior of cast Al A380M and sintered Al 6061 alloys," *Journal of Surface Engineered Materials and Advanced Technology*, vol. 5, p. 1, 2014.
- [74] M. Nazir, Z. A. Khan, and K. Stokes, "Optimisation of interface roughness and coating thickness to maximise coating–substrate adhesion—a failure prediction and reliability assessment modelling," *Journal of Adhesion Science and Technology*, vol. 29, pp. 1415-1445, 2015.
- [75] M. Nazir, Z. A. Khan, A. Saeed, and K. Stokes, "Modeling the Effect of Residual and Diffusion-Induced Stresses on Corrosion at the Interface of Coating and Substrate," *Corrosion*, vol. 72, pp. 500-517, 2015.